Commun. Comput. Phys.
doi: 10.4208/cicp.210815.240316a

Vol. **20**, No. 2, pp. 405-440
August 2016

Direct Calculation of Permeability by High-Accurate Finite Difference and Numerical Integration Methods

Yi Wang[1] and Shuyu Sun[2,*]

[1] *National Engineering Laboratory for Pipeline Safety/MOE Key Laboratory of Petroleum Engineering/Beijing Key Laboratory of Urban Oil and Gas Distribution Technology, China University of Petroleum-Beijing, Beijing 102249, China.*
[2] *Computational Transport Phenomena Laboratory, Division of Physical Science and Engineering, King Abdullah University of Science and Technology, Thuwal 23955-6900, Saudi Arabia.*

Received 21 August 2015; Accepted (in revised version) 24 March 2016

Abstract. Velocity of fluid flow in underground porous media is 6∼12 orders of magnitudes lower than that in pipelines. If numerical errors are not carefully controlled in this kind of simulations, high distortion of the final results may occur [1–4]. To fit the high accuracy demands of fluid flow simulations in porous media, traditional finite difference methods and numerical integration methods are discussed and corresponding high-accurate methods are developed. When applied to the direct calculation of full-tensor permeability for underground flow, the high-accurate finite difference method is confirmed to have numerical error as low as 10^{-5}% while the high-accurate numerical integration method has numerical error around 0%. Thus, the approach combining the high-accurate finite difference and numerical integration methods is a reliable way to efficiently determine the characteristics of general full-tensor permeability such as maximum and minimum permeability components, principal direction and anisotropic ratio.

AMS subject classifications: 76S05

Key words: Finite difference method, numerical integration method, high accuracy, full tensor permeability, stokes.

1 Introduction

Fluid flow in subsurface porous media is quite slow. The flow rate is usually 6∼12 orders of magnitudes lower than the flow in pipes or channels. Thus, this kind of flow

*Corresponding author. *Email addresses:* yiwang1031@gmail.com (Y. Wang), shuyu.sun@kaust.edu.sa (S. Sun)

 ©2016 Global-Science Press

https://doi.org/10.4208/cicp.210815.240316a Published online by Cambridge University Press

can usually be considered as quasi-steady flows at the pore scale. At the field scale, Darcy's law [5] was widely used to describe it and corresponding numerical methods were developed [6–10]. However, modeling of the flow by Darcy's law requires the permeability to be pre-determined [11]. The permeability is often considered as a symmetric full tensor, which contains 3 independent components in two-dimensional (2D) cases and 6 independent components in three-dimensional (3D) cases. This is because numerous practical problems make permeability measurements to be very difficult so that the experiments [12–21] and related models [22–30] are usually limited to the simplified assumptions of isotropy, homogenization or symmetry. These assumptions are practical for simple reservoirs. However, they may bury some important characteristics of real porous media which have complex geometric structures and largely reduce the accuracy of reservoir simulations [25,31,32]. Therefore, cancellation of the simplified assumptions using full-tensor permeability is a better approach. This approach does not require any assumptions on permeability. In our previous study, this new approach was demonstrated by direct-downscaling from Darcy scale to the pore scale described by Navier-Stokes equation [33]. However, the computational speed was not acceptable so that some important factors on permeability such as solid position, porosity and side length ratio were not studied. Thus, we expect to develop a new method with high accuracy and speed.

Since flows in reservoirs are quasi-steady and very slow, the convection terms are so weak that they can be neglected so that this kind of flow can also be simplified to be a steady-state Stokes flow. Therefore, the steady-state Stokes equation is adopted in this study instead of Navier-Stokes equation. The flow driven by gravity with periodic boundary condition used in the previous study [33] is also used in this study. Benchmark solutions of the full-tensor permeability are also important for studying characteristics of complex reservoirs so that they are provided by using this new approach. The details of the new numerical methods with high accuracy are introduced in Section 2 firstly and numerical results are discussed in Section 3.

2 High accurate numerical methods

2.1 High accurate methods for flow simulation

For 2D steady-state Stokes flow with constant fluid properties, we have the governing equations as follows:

$$\frac{\partial u}{\partial x}+\frac{\partial v}{\partial y}=0, \tag{2.1}$$

$$\mu\frac{\partial}{\partial x}\left(\frac{\partial u}{\partial x}\right)+\mu\frac{\partial}{\partial y}\left(\frac{\partial u}{\partial y}\right)-\frac{\partial p}{\partial x}+\rho g_x=0, \tag{2.2}$$

$$\mu\frac{\partial}{\partial x}\left(\frac{\partial v}{\partial x}\right)+\mu\frac{\partial}{\partial y}\left(\frac{\partial v}{\partial y}\right)-\frac{\partial p}{\partial y}+\rho g_y=0, \tag{2.3}$$

https://doi.org/10.4208/cicp.210815.240316a Published online by Cambridge University Press

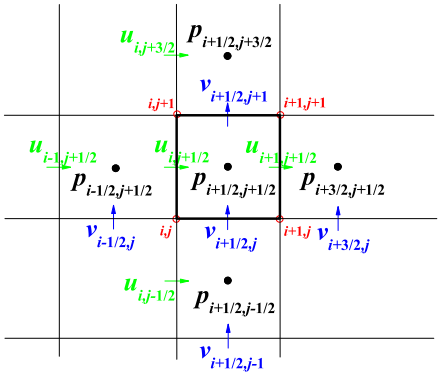


Figure 1: Staggered grid using CCFD.

where u and v are the pore-scale velocity components in the x and y directions, g_x and g_y are the components of gravity, p is the pressure, ρ is the density of the fluid, μ is the dynamic viscosity of the fluid. Eq. (2.1) is the continuity equation. Eqs. (2.2) and (2.3) are the momentum equations in the x and y directions respectively. By using the cell centered finite difference (CCFD) scheme and rectangular staggered grid [34], the computational domain can be discretized in the manner in Fig. 1.

For each grid cell, Eq. (2.1) is discretized on the cell center $(i+1/2,j+1/2)$ while Eqs. (2.2) and (2.3) are discretized on the cell interfaces $(i,j+1/2)$ and $(i+1/2,j)$ respectively. Their discretized forms regardless of solid regions are shown as follows:

$$\frac{u_{i+1,j+1/2}-u_{i,j+1/2}}{x_{i+1}-x_i}+\frac{v_{i+1/2,j+1}-v_{i+1/2,j}}{y_{j+1}-y_j}=0, \tag{2.4}$$

$$\mu\frac{\frac{u_{i+1,j+\frac{1}{2}}-u_{i,j+\frac{1}{2}}}{x_{i+1}-x_i}-\frac{u_{i,j+\frac{1}{2}}-u_{i-1,j+\frac{1}{2}}}{x_i-x_{i-1}}}{x_{i+\frac{1}{2}}-x_{i-\frac{1}{2}}}+\mu\frac{\frac{u_{i,j+\frac{3}{2}}-u_{i,j+\frac{1}{2}}}{y_{j+\frac{3}{2}}-y_{j+\frac{1}{2}}}-\frac{u_{i,j+\frac{1}{2}}-u_{i,j-\frac{1}{2}}}{y_{j+\frac{1}{2}}-y_{j-\frac{1}{2}}}}{y_{j+1}-y_j}$$
$$-\frac{p_{i+\frac{1}{2},j+\frac{1}{2}}-p_{i-\frac{1}{2},j+\frac{1}{2}}}{x_{i+\frac{1}{2}}-x_{i-\frac{1}{2}}}+\rho(g_x)_{i,j+\frac{1}{2}}=0, \tag{2.5}$$

$$\mu\frac{\frac{v_{i+\frac{3}{2},j}-v_{i+\frac{1}{2},j}}{x_{i+\frac{3}{2}}-x_{i+\frac{1}{2}}}-\frac{v_{i+\frac{1}{2},j}-v_{i-\frac{1}{2},j}}{x_{i+\frac{1}{2}}-x_{i-\frac{1}{2}}}}{x_{i+1}-x_i}+\mu\frac{\frac{v_{i+\frac{1}{2},j+1}-v_{i+\frac{1}{2},j}}{y_{j+1}-y_j}-\frac{v_{i+\frac{1}{2},j}-v_{i+\frac{1}{2},j-1}}{y_j-y_{j-1}}}{y_{j+\frac{1}{2}}-y_{j-\frac{1}{2}}}$$
$$-\frac{p_{i+\frac{1}{2},j+\frac{1}{2}}-p_{i+\frac{1}{2},j-\frac{1}{2}}}{y_{j+\frac{1}{2}}-y_{j-\frac{1}{2}}}+\rho\left(g_y\right)_{i+\frac{1}{2},j}=0. \tag{2.6}$$

In the presence of solid regions, non-slip boundary conditions should be considered for the interfaces of fluids and solids so that the discretized forms should be modified.

For better understandings, we explain the modifications using the case in Fig. 2. The gray regions represent the solid regions while the white regions represent the fluid re-

https://doi.org/10.4208/cicp.210815.240316a Published online by Cambridge University Press

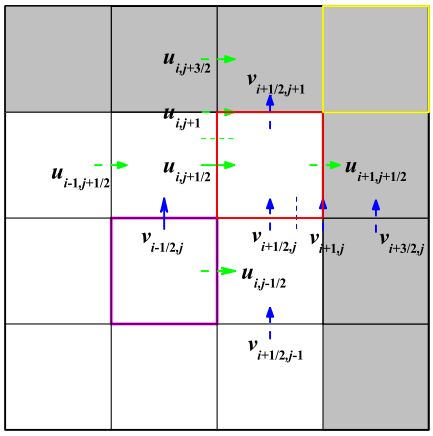


Figure 2: Discretization strategy.

gions. For cells in the solid regions such as the yellow cell, all velocity components in Eq. (2.4) are forced to be zeros and Eqs. (2.5) and (2.6) should be cancelled. For cells completely in the fluid regions such as the purple cell, Eqs. (2.4)-(2.6) can be used directly. For the cells in the fluid regions but adjacent to the solid regions such as the red cell, the velocity components on the solid interfaces are forced to be zeros ($u_{i+1,j+1/2}=0$ and $v_{i+1/2,j+1}=0$) which are similar to the purple cell. The velocity components on the fluid interfaces need to be calculated by the governing equations. It can be easily known from Fig. 2 that the discretized forms of the continuity equation and the second order derivatives in the normal directions ($\frac{\partial}{\partial x}(\frac{\partial u}{\partial x})_{i,j+1/2}$ and $\frac{\partial}{\partial y}(\frac{\partial v}{\partial y})_{i+1/2,j}$) in the momentum equations are still the same as Eqs. (2.4)-(2.6) respectively. However, due to the existence of the solid regions, it may be not accurate enough to discretize the second order derivatives in the tangential directions ($\frac{\partial}{\partial y}(\frac{\partial u}{\partial y})_{i,j+1/2}$ and $\frac{\partial}{\partial x}(\frac{\partial v}{\partial x})_{i+1/2,j}$) in the manner of Eqs. (2.5) and (2.6) so that modifications are needed. The original discretization and its two modifications are named Algorithm 1.1, Algorithm 1.2, Algorithm 1.3 as follows.

Algorithm 1.1: In this algorithm, the effect of solid walls on the discretization is completely not considered. As shown in Eqs. (2.5) and (2.6), the derivatives are approximated using the adjacent velocity components $u_{i,j-1/2}$, $u_{i,j+1/2}$, $u_{i,j+3/2}$ and $u_{i-1/2,j}$, $u_{i+1/2,j}$, $u_{i+3/2,j}$ directly:

$$\frac{\partial}{\partial y}\left(\frac{\partial u}{\partial y}\right)_{i,j+\frac{1}{2}}=\frac{\frac{u_{i,j+\frac{3}{2}}-u_{i,j+\frac{1}{2}}}{y_{j+\frac{3}{2}}-y_{j+\frac{1}{2}}}-\frac{u_{i,j+\frac{1}{2}}-u_{i,j-\frac{1}{2}}}{y_{j+\frac{1}{2}}-y_{j-\frac{1}{2}}}}{y_{j+1}-y_j}, \tag{2.7}$$

$$\frac{\partial}{\partial x}\left(\frac{\partial v}{\partial x}\right)_{i+\frac{1}{2},j}=\frac{\frac{v_{i+\frac{3}{2},j}-v_{i+\frac{1}{2},j}}{x_{i+\frac{3}{2}}-x_{i+\frac{1}{2}}}-\frac{v_{i+\frac{1}{2},j}-v_{i-\frac{1}{2},j}}{x_{i+\frac{1}{2}}-x_{i-\frac{1}{2}}}}{x_{i+1}-x_i}. \tag{2.8}$$

https://doi.org/10.4208/cicp.210815.240316a Published online by Cambridge University Press

Algorithm 1.2: This algorithm is usually used. The adjacent velocity components, if they are located in the solid regions ($u_{i,j+3/2}$ and $v_{i+3/2,j}$), are replaced by the velocity components at the interfaces of fluid regions and solid regions ($u_{i,j+1}$ and $v_{i+1,j}$):

$$\frac{\partial}{\partial y}\left(\frac{\partial u}{\partial y}\right)_{i,j+\frac{1}{2}}=\frac{\frac{u_{i,j+1}-u_{i,j+\frac{1}{2}}}{y_{j+1}-y_{j+\frac{1}{2}}}-\frac{u_{i,j+\frac{1}{2}}-u_{i,j-\frac{1}{2}}}{y_{j+\frac{1}{2}}-y_{j-\frac{1}{2}}}}{y_{j+1}-y_j}, \tag{2.9}$$

$$\frac{\partial}{\partial x}\left(\frac{\partial v}{\partial x}\right)_{i+\frac{1}{2},j}=\frac{\frac{v_{i+1,j}-v_{i+\frac{1}{2},j}}{x_{i+1}-x_{i+\frac{1}{2}}}-\frac{v_{i+\frac{1}{2},j}-v_{i-\frac{1}{2},j}}{x_{i+\frac{1}{2}}-x_{i-\frac{1}{2}}}}{x_{i+1}-x_i}. \tag{2.10}$$

Algorithm 1.3: In the above two algorithms, we actually calculate all the first-order derivatives on the interfaces of the grid cells. Here, we propose a new method via shifting the first-order derivatives $1/4$ grid spacing from the interfaces toward the grid centers if the interfaces are between fluids and solids:

$$\frac{\partial}{\partial y}\left(\frac{\partial u}{\partial y}\right)_{i,j+\frac{1}{2}}=\frac{\frac{u_{i,j+1}-u_{i,j+\frac{1}{2}}}{y_{j+1}-y_{j+\frac{1}{2}}}-\frac{u_{i,j+\frac{1}{2}}-u_{i,j-\frac{1}{2}}}{y_{j+\frac{1}{2}}-y_{j-\frac{1}{2}}}}{y_{j+\frac{3}{4}}-y_j}, \tag{2.11}$$

$$\frac{\partial}{\partial x}\left(\frac{\partial v}{\partial x}\right)_{i+\frac{1}{2},j}=\frac{\frac{v_{i+1,j}-v_{i+\frac{1}{2},j}}{x_{i+1}-x_{i+\frac{1}{2}}}-\frac{v_{i+\frac{1}{2},j}-v_{i-\frac{1}{2},j}}{x_{i+\frac{1}{2}}-x_{i-\frac{1}{2}}}}{x_{i+\frac{3}{4}}-x_i}. \tag{2.12}$$

Combining the discretized equations (2.4)-(2.12), we can obtain the matrix equation by converting the above coefficients to the form of matrix A and vector b: $A\boldsymbol{x}=b$. The solution $\boldsymbol{x}=[\boldsymbol{u}\ \boldsymbol{v}\ \boldsymbol{p}]^T$ can be obtained by directly solving this matrix equation using MATLAB. The matrix equation is linear so that the solving process is very fast by using the MATLAB function $\boldsymbol{x}=A\backslash b$.

To validate the code and select the most accurate algorithm from the three Algorithms 1.1-1.3, we block two ends of the domain (Fig. 3) so that the case becomes a Posullie flow, which has analytical solutions.

In Fig. 3, the white areas represent the fluid regions while the black areas represent the solid regions. For simplification, the domain size is set as $L=1$m and the fluid properties are set as: $\rho=1kg/m^3$, $\mu=1Pa\cdot s$. Then the analytical solution of the pore-scale velocity is:

$$v=\begin{cases}\frac{1}{2}x^2-\frac{1}{2}x+\frac{3}{32}, & \frac{1}{4}\le x\le\frac{3}{4},\\ 0, & \text{other.}\end{cases} \tag{2.13}$$

The mean deviation of the results of each algorithm from the analytical solution is defined as:

$$\sigma=\frac{\sum_{j=1}^{ny}\sum_{i=1}^{nx}\left|\frac{v_{i,j}-v_{i,j}^{analy}}{v_{i,j}^{analy}}\right|}{nx\cdot ny}\times 100\%, \tag{2.14}$$

https://doi.org/10.4208/cicp.210815.240316a Published online by Cambridge University Press

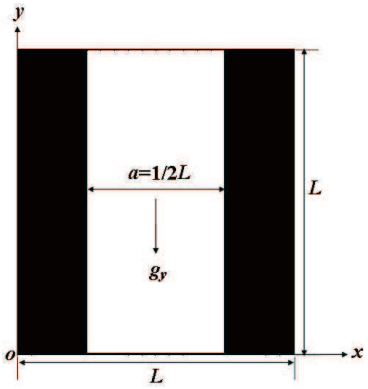


Figure 3: Poiseuile Flow.

where $v_{i,j}^{analy}$ is the analytical velocity, $v_{i,j}$ is the velocity obtained by each algorithm, nx and ny are the grid numbers in the x and y directions respectively. It is clear in Table 1 that the deviation created by Algorithm 1.1 is too high. It decreases with grid number very slowly. The deviation still remains as high as 18.2% when the grid number is as much as 60×60. Thus, it is hard to expect Algorithm 1.1 can obtain accurate solutions even on denser grids. This is the reason why the discretizations of the tangential derivatives should be modified. Algorithm 1.2 is a commonly used scheme. It is much more accurate and converges with grid number much faster than Algorithm 1.1 (2.1%-0.3%). Thus, this algorithm can satisfy the accuracy demand of many applications. The deviation of Algorithm 1.3 from the analytical solution is only 1.4×10^{-5}% even using the grid number as low as 20×20. This accuracy beats the other two algorithms. Moreover, the deviation becomes stable only after two refinements of grids, which are not achieved by Algorithm 1.1 and Algorithm 1.2. Thus, Algorithm 1.3 is the best scheme with the highest accuracy and the best convergence.

Table 1: Mean deviations of Algorithms 1.1-1.3 from the analytical solution.

Schemes	Grid number		
	20×20	40×40	60×60
Algorithm 1.1	44.8%	25.4%	18.2%
Algorithm 1.2	2.1%	0.6%	0.3%
Algorithm 1.3	1.4×10^{-5}%	1.3×10^{-5}%	1.3×10^{-5}%

2.2 High accurate methods for permeability calculation

Permeability obeys the Darcy/s law:

$$\mathbf{u}^D = -\frac{\mathbf{k}}{\mu}(\nabla p - \rho\mathbf{g}), \tag{2.15}$$

https://doi.org/10.4208/cicp.210815.240316a Published online by Cambridge University Press

where $\mathbf{u}^D=\begin{bmatrix}u_x^D\\u_y^D\end{bmatrix}$ is the Darcy velocity, $\mathbf{k}=\begin{bmatrix}k_{xx}&k_{xy}\\k_{yx}&k_{yy}\end{bmatrix}$ is the full-tensor permeability, $\mathbf{g}=\begin{bmatrix}g_x\\g_y\end{bmatrix}$ is the gravity, ∇p is the pressure gradient, ρ is the density of the fluid, and μ is the dynamic viscosity of the fluid. No assumptions are made for the components of the full tensor so that all the four values k_{xx}, k_{yy}, k_{xy} and k_{yx} are only obtained by calculation independently. Eq. (2.15) is in the scale of the whole computational domain which is different from Eqs. (2.1)-(2.3) in the scale of grid cells. Therefore, ∇p in Eq. (2.15) is zero due to the periodic boundary conditions, and the Darcy velocity is actually the volumetric mean velocity of the whole domain so that Eq. (2.15) becomes:

$$\overline{\mathbf{u}}=\frac{\rho}{\mu}\mathbf{k}\mathbf{g}, \tag{2.16}$$

where $\overline{\mathbf{u}}=\frac{1}{V}\int_V \mathbf{u}dV$, $\mathbf{u}=\begin{bmatrix}u_x\\u_y\end{bmatrix}$, $\overline{\mathbf{u}}=\begin{bmatrix}\overline{u_x}\\\overline{u_y}\end{bmatrix}$, V is the whole volume of the domain. Substituting these expressions to Eq.(16), we can obtain:

$$\begin{bmatrix}\overline{u_x}\\\overline{u_y}\end{bmatrix}=\frac{\rho}{\mu}\begin{bmatrix}k_{xx}&k_{xy}\\k_{yx}&k_{yy}\end{bmatrix}\begin{bmatrix}g_x\\g_y\end{bmatrix}. \tag{2.17}$$

If we obtain samples in the condition of $g_x=g$, $g_y=0$, Eq. (2.17) becomes:

$$\begin{bmatrix}(\overline{u_x})_{g_x=g}\\(\overline{u_y})_{g_x=g}\end{bmatrix}=\frac{\rho g}{\mu}\begin{bmatrix}k_{xx}\\k_{yx}\end{bmatrix}. \tag{2.18}$$

If we obtain samples in the condition of $g_x=0$, $g_y=g$, Eq. (2.17) becomes:

$$\begin{bmatrix}(\overline{u_x})_{g_y=g}\\(\overline{u_y})_{g_y=g}\end{bmatrix}=\frac{\rho g}{\mu}\begin{bmatrix}k_{xy}\\k_{yy}\end{bmatrix}. \tag{2.19}$$

From Eqs. (2.18) and (2.19), we can obtain:

$$\begin{bmatrix}k_{xx}&k_{xy}\\k_{yx}&k_{yy}\end{bmatrix}=\frac{\mu}{\rho g}\begin{bmatrix}(\overline{u_x})_{g_x=g}&(\overline{u_x})_{g_y=g}\\(\overline{u_y})_{g_x=g}&(\overline{u_y})_{g_y=g}\end{bmatrix}. \tag{2.20}$$

The full-tensor permeability can be calculated by Eq. (2.20).

To obtain the principal directions and anisotropic ratios for any cases, we expect to transform any full tensor of permeability to the diagonal form named effective permeability tensor. This can be fulfilled by the eigenvalue problem as follows:

$$\mathbf{k}=\mathbf{V}\mathbf{k}_{eff}\mathbf{V}^{-1}, \tag{2.21}$$

https://doi.org/10.4208/cicp.210815.240316a Published online by Cambridge University Press

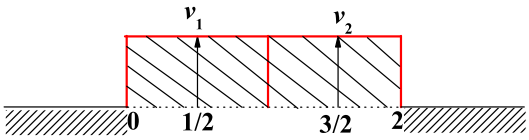


Figure 4: Rectangular integration.

where $\mathbf{k}_{eff}=\begin{bmatrix} k_{\max} & 0 \\ 0 & k_{\min} \end{bmatrix}$, $\mathbf{V}=\begin{bmatrix} \mathrm{v}_{1,1} & \mathrm{v}_{1,2} \\ \mathrm{v}_{2,1} & \mathrm{v}_{2,2} \end{bmatrix}$ is the matrix consist of orthogonal eigenvectors, $k_{\max}$ is the maximum component of the effective permeability in the principal direction, $k_{\min}$ is the minimum component of the effective permeability orthogonal to the principal direction. Other characteristic values of the effective permeability tensor can be defined as follows:

$$\xi = k_{\max}/k_{\min}, \tag{2.22}$$

$$\alpha = \arctan(\mathrm{v}_{2,1}/\mathrm{v}_{1,1}), \tag{2.23}$$

where ξ is the anisotropic ratio which represents the degree of anisotropy, α is the angle between the direction with $k_{\max}$ and the x direction. Thus, it represents the so-called principal direction.

It can be easily seen in Eq. (2.20) that the accuracy of full-tensor permeability is completely determined by the four components of the volumetric mean velocity. For most real cases, they have no analytical solutions so that the volumetric integration in Eq. (2.16) cannot be calculated directly and numerical integrations should be used to approximate it. The most common way is using the rectangular integration method. It is named Algorithm 2.1 here. We also proposed a new method named Algorithm 2.2 to promote accuracy. They are compared using the Poiseuile flow with only two grids as shown in Fig. 4 and Fig. 5. The analytical solutions are $v=\frac{1}{2}x^2-x$ and $v_1=v_2=-\frac{3}{8}m/s$. Thus, the mean velocity by the analytical solutions is $\overline{v}=-\frac{1}{3}m/s$. The two algorithms of numerical integration are explained as follows:

Algorithm 2.1: Rectangular integration is used for the whole domain as shown in Fig. 4:

$$\int_V v dV = v_1 + v_2. \tag{2.24}$$

Algorithm 2.2: We divide the whole integration into several sub-domains. Each sub-domain uses a high-order polynomial covering this sub-domain and part of the neighboring sub-domains. If a sub-domain is adjacent to the solid region, the polynomial does not include the grid points inside the solid region but includes the fluid-solid interfaces. For example, the integrations within the sub-domains [0,1] and [1,2] use the polynomials containing three points ($x=0$, $x=1/2$, $x=3/2$ in Fig. 5(a) and $x=1/2$, $x=3/2$, $x=2$ in Fig. 5(b)). The expressions for the integrations are:

$$\int_V v dV = \int_0^1 (a_1x^2+b_1x+c_1)\,dx + \int_1^2 (a_2x^2+b_2x+c_2)\,dx, \tag{2.25}$$

https://doi.org/10.4208/cicp.210815.240316a Published online by Cambridge University Press

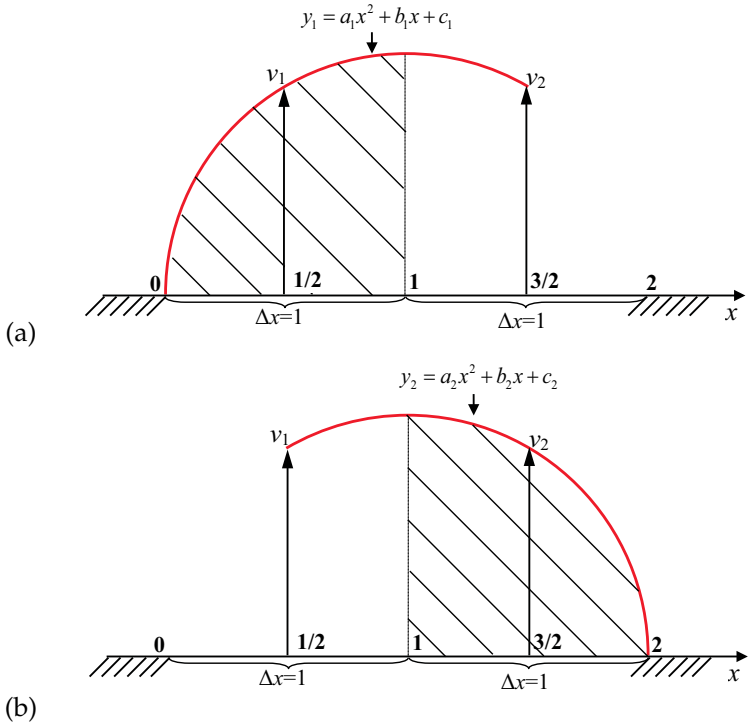


Figure 5: High-order sub-domain integration: (a) Integration in sub-domain [0,1]; (b) Integration in sub-domain [1,2].

where $a_1=-2v_1+\frac{2}{3}v_2$, $b_1=3v_1-\frac{1}{3}v_2$, $c_1=0$, $a_2=\frac{2}{3}v_1-2v_2$, $b_2=-\frac{7}{3}v_1+5v_2$, $c_2=2v_1-2v_2$. Substituting these parameters to Eq. (2.25), we can obtain the final expression:

$$\int_V vdV=\frac{8}{9}(v_1+v_2). \tag{2.26}$$

Thus, by using the analytical solutions of v_1 and v_2, the mean velocity calculated by Algorithm 2.1 is:

$$\overline{v_{2.1}}=\frac{1}{V}\int_V vdV=\frac{1}{2}(v_1+v_2)=-\frac{3}{8}m/s. \tag{2.27}$$

The mean velocity calculated by Algorithm 2.2 is:

$$\overline{v_{2.2}}=\frac{1}{V}\int_V vdV=\frac{1}{2}\cdot\frac{8}{9}(v_1+v_2)=-\frac{1}{3}m/s. \tag{2.28}$$

Apparently, the rectangular integration may cause the mean velocity (Darcy velocity) deviate from the analytical solution as much as 12.5% even if the analytical solutions of the pore-scale velocity are used. On the other hand, our new integration method can obtain the results having no error with the analytical solution so that it is much more accurate.

https://doi.org/10.4208/cicp.210815.240316a Published online by Cambridge University Press

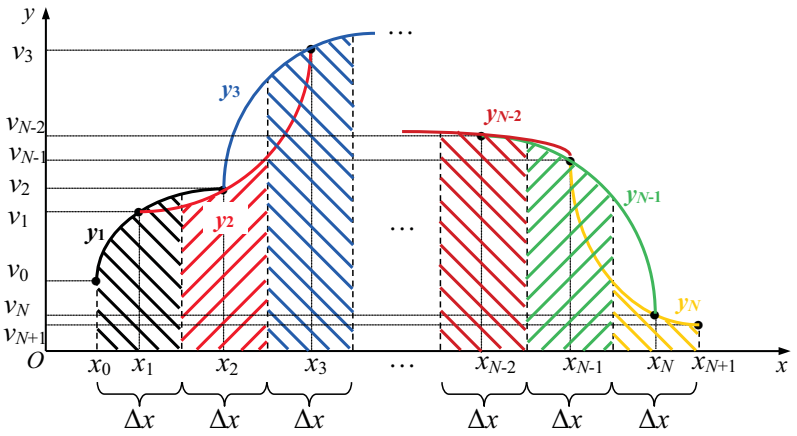


Figure 6: General form of the high-order sub-domain integration.

The above comparison case is quite simple: 1) the expression of velocity ($v=\frac{1}{2}x^2-x$) is quadratic while the quadratic polynomials are also utilized in the new integration method; 2) the computational domain is restricted to [0,2]; 3) the domain is discretized into only two grids. Thus the simple case cannot support the comparison conclusion sufficiently. To further prove the advantage of the new integration method, we expand the Algorithm 2.2 to a general form in Fig. 6, where the general domain $[x_0,x_{N+1}]$ divided by N grids with uniform grid length Δx are defined. $x_1\sim x_N$ are the center of each grid due to CCFD while x_0 and x_{N+1} are boundary points. The quadratic polynomial $y_n=a_nx^2+b_nx+c_n$ ($n=1,\cdots,N$) is constructed and then integrated in the corresponding sub-domain so that the total integration can be obtained by summing all the integrations in the sub-domains as shown in Eq. (2.29). The details of the derivation can be found in Appendix A.

$$\int_V vdV=\Delta x\sum_{n=0}^{N+1}\beta_n v_n, \tag{2.29}$$

where

$$\begin{aligned}
&N=1\colon\ \beta_0=\beta_{N+1}=\frac{1}{6},\ \beta_1=\frac{2}{3},\\
&N=2\colon\ \beta_0=\beta_{N+1}=\frac{1}{9},\ \beta_1=\beta_N=\frac{8}{9},\\
&N=3\colon\ \beta_0=\beta_{N+1}=\frac{1}{9},\ \beta_1=\beta_N=\frac{7}{8},\ \beta_2=\frac{37}{36},\\
&N=4\colon\ \beta_0=\beta_{N+1}=\frac{1}{9},\ \beta_1=\beta_N=\frac{7}{8},\ \beta_2=\beta_{N-1}=\frac{73}{72},\\
&N\geq 5\colon\ \beta_0=\beta_{N+1}=\frac{1}{9},\ \beta_1=\beta_N=\frac{7}{8},\ \beta_2=\beta_{N-1}=\frac{73}{72},\ \beta_3=\cdots=\beta_{N-2}=1.
\end{aligned}$$

https://doi.org/10.4208/cicp.210815.240316a Published online by Cambridge University Press

Table 2: Deviations of mean velocity calculated by Algorithm 2.1.

N	$v=x$	$v=x^3$	$v=x^4$	$v=1/(1+x)$	$v=\sin x$	$v=\tan x$	$v=e^x$
1	0.0000%	50.0000%	68.7500%	3.8203%	4.2915%	11.2607%	4.0483%
2	0.0000%	12.5000%	19.9219%	1.0723%	1.0493%	3.5991%	1.0341%
3	0.0000%	5.5556%	9.0792%	0.4894%	0.4645%	1.7094%	0.4615%
4	0.0000%	3.1250%	5.1514%	0.2780%	0.2609%	0.9875%	0.2599%
5	0.0000%	2.0000%	3.3100%	0.1788%	0.1669%	0.6404%	0.1665%
6	0.0000%	1.3889%	2.3036%	0.1245%	0.1158%	0.4480%	0.1156%
7	0.0000%	1.0204%	1.6946%	0.0916%	0.0851%	0.3307%	0.0850%
8	0.0000%	0.7812%	1.2985%	0.0702%	0.0651%	0.2539%	0.0651%
9	0.0000%	0.6173%	1.0266%	0.0555%	0.0515%	0.2011%	0.0514%
10	0.0000%	0.5000%	0.8319%	0.0450%	0.0417%	0.1631%	0.0417%
60	0.0000%	0.0139%	0.0231%	0.0013%	0.0012%	0.0046%	0.0012%
100	0.0000%	0.0050%	0.0083%	0.0005%	0.0004%	0.0016%	0.0004%

The volume of the domain is $V=N\Delta x$ so that the mean velocity computed from Eq. (2.29) is:

$$\overline{v_{2.2}}=\frac{1}{N}\sum_{n=0}^{N+1}\beta_n v_n. \tag{2.30}$$

Setting 7 velocity functions ($v=x$, x^3, x^4, $1/(1+x)$, $\sin x$, $\tan x$, e^x) and letting $x_0=0$, $x_{N+1}=1$, $N=1,\cdots,100$, we can calculate the mean velocity of each function using both Algorithm 2.1 and Algorithm 2.2 and compare it with the analytical solution (0.5, 0.25, 0.2, 0.69, 0.46, 0.62, 1.72 for the 7 velocity functions respectively). The corresponding deviations from the analytical solutions are shown in Table 2 and Table 3 respectively. It is apparently shown that Algorithm 2.2 has overall 1∼3 orders of magnitudes higher than Algorithm 2.1. Moreover, Algorithm 2.2 can achieve high accuracy even on very coarse grid (maximum deviation as low as 4.1667% compared with 68.75% by Algorithm 2.1) and converges with grid number very fast (nearly 0% deviation after $N=10$). These results verify that Algorithm 2.2 has much higher accuracy than Algorithm 2.1 not only for quadratic distribution of velocity but also for many other distribution functions so that it is much better than Algorithm 2.1.

Applying Eq. (2.30) to every direction of the two-dimensional domain of porous media (Fig. 2), we can easily obtain the general form of the Darcy velocity as follows:

$$u_x^D=\frac{1}{N_x+1}\sum_{i=0}^{N_x}\left(\frac{1}{N_y}\sum_{j=0}^{N_y+1}\alpha_j u_{i,j}\right), \tag{2.31}$$

$$u_y^D=\frac{1}{N_y+1}\sum_{j=0}^{N_y}\left(\frac{1}{N_x}\sum_{i=0}^{N_x+1}\beta_i v_{i,j}\right), \tag{2.32}$$

where α_j and β_i have the same expression with β_n in Eq. (2.29).

https://doi.org/10.4208/cicp.210815.240316a Published online by Cambridge University Press

Table 3: Deviations of mean velocity calculated by Algorithm 2.2.

N	$v=x$	$v=x^3$	$v=x^4$	$v=1/(1+x)$	$v=\sin x$	$v=\tan x$	$v=e^x$
1	0.0000%	0.0000%	4.1667%	0.1872%	0.0358%	1.3227%	0.0337%
2	0.0000%	0.0000%	1.0417%	0.0418%	0.0090%	0.2559%	0.0084%
3	0.0000%	0.0000%	0.3344%	0.0152%	0.0029%	0.107%	0.0027%
4	0.0000%	0.0000%	0.1261%	0.0062%	0.0011%	0.0475%	0.0010%
5	0.0000%	0.0000%	0.0567%	0.0029%	0.0005%	0.0238%	0.0005%
6	0.0000%	0.0000%	0.0289%	0.0016%	0.0002%	0.0132%	0.0002%
7	0.0000%	0.0000%	0.0162%	0.0009%	0.0001%	0.0079%	0.0001%
8	0.0000%	0.0000%	0.0098%	0.0006%	0.0001%	0.0050%	0.0001%
9	0.0000%	0.0000%	0.0062%	0.0004%	0.0001%	0.0033%	0.0001%
10	0.0000%	0.0000%	0.0042%	0.0002%	0.0000%	0.0023%	0.0000%
60	0.0000%	0.0000%	0.0000%	0.0000%	0.0000%	0.0000%	0.0000%
100	0.0000%	0.0000%	0.0000%	0.0000%	0.0000%	0.0000%	0.0000%

3 Results and discussion

According to Section 2, the newly proposed schemes, Algorithm 1.3 and Algorithm 2.2, are examined to be the high-accurate methods. They also converge with grid number very fast. Thus, we convince that the combination of Algorithm 1.3 and Algorithm 2.2 can achieve high-accurate grid-independent solutions for complex cases more easily. By using the combination of the high-accurate methods, full-tensor permeability are calculated directly from Stokes equation in the computational domain shown in Fig. 7. The grid number is set as 60×60. The periodic boundary conditions are adopted for both the x and y directions. For generalization, the parameters are set as: $\rho=1kg/m^3$, $\mu=1Pa\cdot s$, $g=1m/s^2$, $L=1m$. Then all permeability becomes the times of L^2. The relations of solid

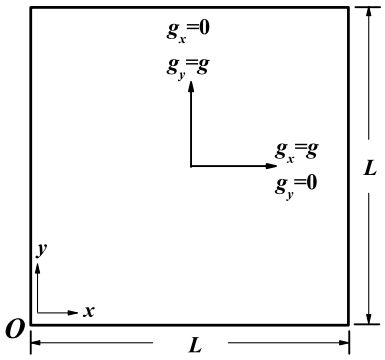


Figure 7: Computational domain and sampling.

https://doi.org/10.4208/cicp.210815.240316a Published online by Cambridge University Press

position, porosity, and side length ratio with permeability are discussed firstly. Results of 90 different porous media are then given.

3.1 Validation of the new high-accurate methods for the calculation of permeability

Two structures of porous media are used as test cases for the calculation of permeability. For case 1 shown in Fig. 8, the numerical errors of traditional methods are decreasing form 40.5% to 4.2% with grid number increasing from 10×10 to 90×90. The numerical error of the new methods is only 0.7% for the mesh 10×10 and decreases to 0% rapidly from the mesh 20×20 (Table 4). Similar trend also occurs for case 2 in Fig. 9 and Table 5. Thus, the high-accurate methods developed in this paper are also much better than the traditional methods for the calculation of permeability.

Table 4: Comparison of permeability for test case 1.

Grid number	Analytical solutions	Traditional methods	Errors	New methods	Errors
10×10	0.0427 0.0000 0.0000 0.0000	0.0600 0.0000 0.0000 0.0000	40.5%	0.0430 0.0000 0.0000 0.0000	0.7%
20×20	0.0427 0.0000 0.0000 0.0000	0.0510 0.0000 0.0000 0.0000	19.4%	0.0427 0.0000 0.0000 0.0000	0%
30×30	0.0427 0.0000 0.0000 0.0000	0.0481 0.0000 0.0000 0.0000	12.6%	0.0427 0.0000 0.0000 0.0000	0%
40×40	0.0427 0.0000 0.0000 0.0000	0.0468 0.0000 0.0000 0.0000	9.6%	0.0427 0.0000 0.0000 0.0000	0%
50×50	0.0427 0.0000 0.0000 0.0000	0.0459 0.0000 0.0000 0.0000	7.5%	0.0427 0.0000 0.0000 0.0000	0%
60×60	0.0427 0.0000 0.0000 0.0000	0.0454 0.0000 0.0000 0.0000	6.3%	0.0427 0.0000 0.0000 0.0000	0%
70×70	0.0427 0.0000 0.0000 0.0000	0.0450 0.0000 0.0000 0.0000	5.4%	0.0427 0.0000 0.0000 0.0000	0%
80×80	0.0427 0.0000 0.0000 0.0000	0.0447 0.0000 0.0000 0.0000	4.7%	0.0427 0.0000 0.0000 0.0000	0%
90×90	0.0427 0.0000 0.0000 0.0000	0.0445 0.0000 0.0000 0.0000	4.2%	0.0427 0.0000 0.0000 0.0000	0%

3.2 Effect of solid position

A single square solid with side length Δx and Δy, as shown in Fig. 10, is selected firstly to study the solid position effect of permeability. The solid position is defined by the coordinate of solid center: $x_i=(i-0.5)\Delta x$, $y_j=(j-0.5)\Delta y$ ($\Delta x=\Delta y=L/60$). The serial number of solids can be represented by N_k with $k=i+60(j-1)$ ($i=j=60$). The total $60\times60=3600$ positions are used for calculation. Corresponding results are shown in Fig. 11. It is clear that $k_{\max}$ and ξ are all constants with the values $0.1193L^2$ and 1.0000 for different positions.

https://doi.org/10.4208/cicp.210815.240316a Published online by Cambridge University Press

Table 5: Comparison of permeability for test case 2.

Grid number	Analytical solutions	Traditional methods	Errors	New methods	Errors
10×10	$\begin{bmatrix} 0.0000 & 0.0000 \\ 0.0000 & 6.6667\times10^{-4} \end{bmatrix}$	$\begin{bmatrix} 0.0000 & 0.0000 \\ 0.0000 & 0.0020 \end{bmatrix}$	200.0%	$\begin{bmatrix} 0.0000 & 0.0000 \\ 0.0000 & 7.5000\times10^{-4} \end{bmatrix}$	12.5%
20×20	$\begin{bmatrix} 0.0000 & 0.0000 \\ 0.0000 & 6.6667\times10^{-4} \end{bmatrix}$	$\begin{bmatrix} 0.0000 & 0.0000 \\ 0.0000 & 0.0013 \end{bmatrix}$	95.0%	$\begin{bmatrix} 0.0000 & 0.0000 \\ 0.0000 & 6.8750\times10^{-4} \end{bmatrix}$	3.1%
30×30	$\begin{bmatrix} 0.0000 & 0.0000 \\ 0.0000 & 6.6667\times10^{-4} \end{bmatrix}$	$\begin{bmatrix} 0.0000 & 0.0000 \\ 0.0000 & 0.0010 \end{bmatrix}$	50.0%	$\begin{bmatrix} 0.0000 & 0.0000 \\ 0.0000 & 6.7593\times10^{-4} \end{bmatrix}$	1.4%
40×40	$\begin{bmatrix} 0.0000 & 0.0000 \\ 0.0000 & 6.6667\times10^{-4} \end{bmatrix}$	$\begin{bmatrix} 0.0000 & 0.0000 \\ 0.0000 & 9.3750\times10^{-4} \end{bmatrix}$	40.6%	$\begin{bmatrix} 0.0000 & 0.0000 \\ 0.0000 & 6.7188\times10^{-4} \end{bmatrix}$	0.78%
50×50	$\begin{bmatrix} 0.0000 & 0.0000 \\ 0.0000 & 6.6667\times10^{-4} \end{bmatrix}$	$\begin{bmatrix} 0.0000 & 0.0000 \\ 0.0000 & 8.8000\times10^{-4} \end{bmatrix}$	32.0%	$\begin{bmatrix} 0.0000 & 0.0000 \\ 0.0000 & 6.7000\times10^{-4} \end{bmatrix}$	0.5%
60×60	$\begin{bmatrix} 0.0000 & 0.0000 \\ 0.0000 & 6.6667\times10^{-4} \end{bmatrix}$	$\begin{bmatrix} 0.0000 & 0.0000 \\ 0.0000 & 8.4259\times10^{-4} \end{bmatrix}$	26.4%	$\begin{bmatrix} 0.0000 & 0.0000 \\ 0.0000 & 6.6898\times10^{-4} \end{bmatrix}$	0.3%
70×70	$\begin{bmatrix} 0.0000 & 0.0000 \\ 0.0000 & 6.6667\times10^{-4} \end{bmatrix}$	$\begin{bmatrix} 0.0000 & 0.0000 \\ 0.0000 & 8.1633\times10^{-4} \end{bmatrix}$	22.4%	$\begin{bmatrix} 0.0000 & 0.0000 \\ 0.0000 & 6.6837\times10^{-4} \end{bmatrix}$	0.25%
80×80	$\begin{bmatrix} 0.0000 & 0.0000 \\ 0.0000 & 6.6667\times10^{-4} \end{bmatrix}$	$\begin{bmatrix} 0.0000 & 0.0000 \\ 0.0000 & 7.9687\times10^{-4} \end{bmatrix}$	19.5%	$\begin{bmatrix} 0.0000 & 0.0000 \\ 0.0000 & 6.6797\times10^{-4} \end{bmatrix}$	0.19%
90×90	$\begin{bmatrix} 0.0000 & 0.0000 \\ 0.0000 & 6.6667\times10^{-4} \end{bmatrix}$	$\begin{bmatrix} 0.0000 & 0.0000 \\ 0.0000 & 7.8189\times10^{-4} \end{bmatrix}$	17.3%	$\begin{bmatrix} 0.0000 & 0.0000 \\ 0.0000 & 6.6770\times10^{-4} \end{bmatrix}$	0.15%

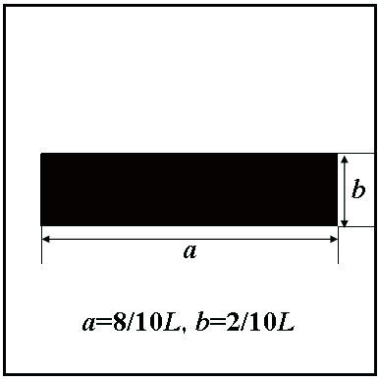


Figure 8: Test case 1.

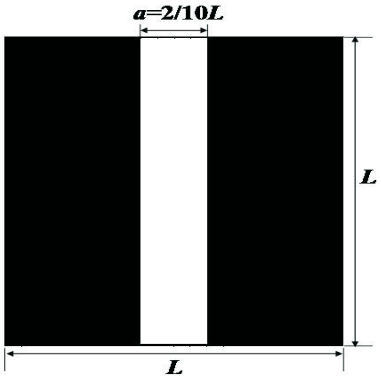


Figure 9: Test case 2.

Another case is double-solid system (Fig. 12) with the same dimension of the above solids. Corresponding results are shown in Fig. 13. The solid position is defined by the geometric center of the system. $x_i = i\Delta x$, $y_j = j\Delta y$, $k = i+60(j-1)$. The results also show that $k_{\max}$, ξ and α are all constants. Their values are $0.0908L^2$, 1.3172 and 45° respectively.

These two cases indicate that the position of the solids does not affect the results for both isotropic cases (Fig. 10) and anisotropic cases (Fig. 12), i.e. the position has no relation with permeability ($k_{\max}$ and $k_{\min}$) and corresponding parameters (ξ and α). Therefore, the following sections will put the solids at the center of the domain.

https://doi.org/10.4208/cicp.210815.240316a Published online by Cambridge University Press

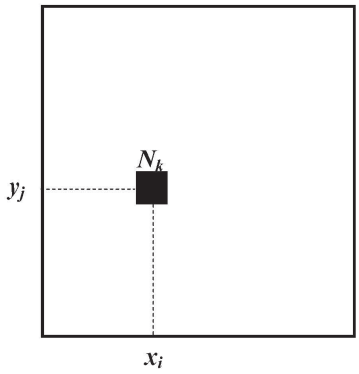


Figure 10: Position effect using single solid.

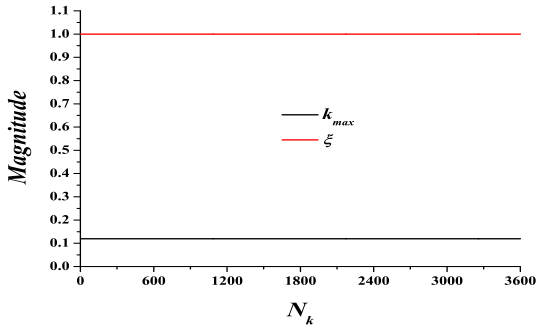


Figure 11: Results for single solid.

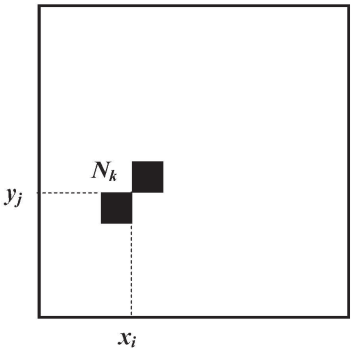


Figure 12: Position effect using double solids.

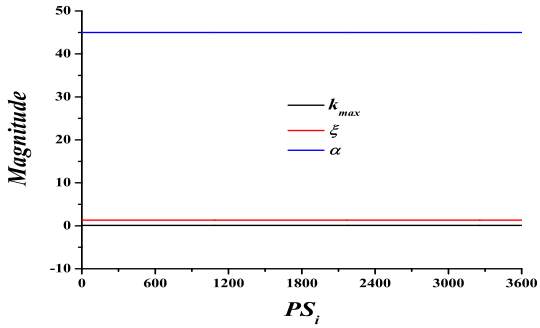


Figure 13: Results for double solids.

3.3 Effect of porosity

Here, porosity is defined as:

$$\phi = 1 - \frac{ab}{L^2}, \tag{3.1}$$

where ϕ is porosity, a and b are side lengths of a solid, L is the side length of the computational domain. As shown in Fig. 14, a set of square solids with side length a are selected to study the porosity effect firstly. $a=b=(2i/60)L$, $i=1,2,3,\cdots,30$. Their permeability tensors are all diagonal, indicating that they are all isotropic. Thus, we can use one symbol k in Fig. 15 to represent the permeability. The permeability is monotonic with porosity. Their relation is nearly linear in the logarithmic coordinate in Fig. 15(b).

Then we use rectangular solids instead of the square solids to further study the porosity effect (Fig. 16). $a=(4i/60)L$ ($i=1,2,3,\cdots,15$), $b=(2+20j)/60L$ ($j=0,1,2$). The corresponding results in Fig. 17 show apparent anisotropic features. The parameters ($k_{\max}$, $k_{\min}$, ξ, α) are no longer a monotonic function of porosity. They can hardly be described by a single function of porosity because the curves in different ranges of porosity are discontinued and partly overlap with each other.

https://doi.org/10.4208/cicp.210815.240316a Published online by Cambridge University Press

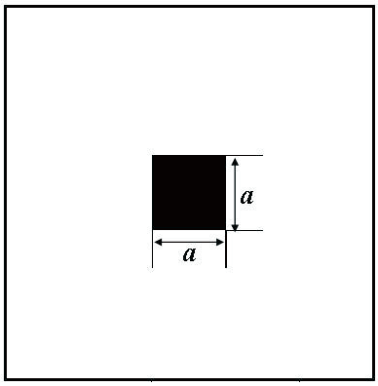
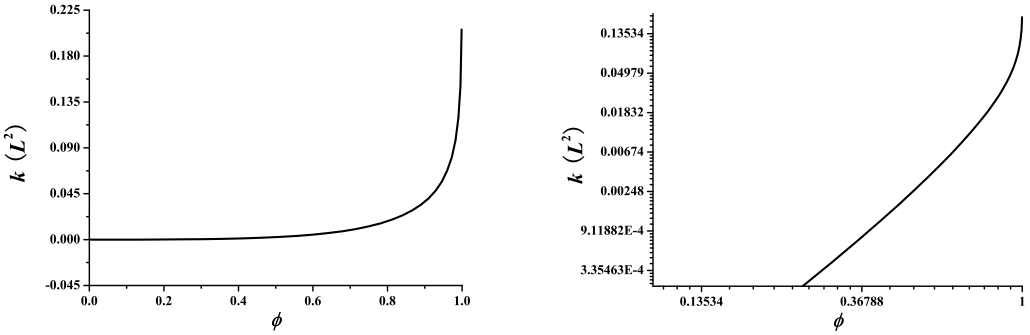


Figure 14: Porosity effect using a square solid.



(a) (b)

Figure 15: Results for different porosities using a square solid: (a) Uniform coordinate; (b) Logarithmic coordinate.

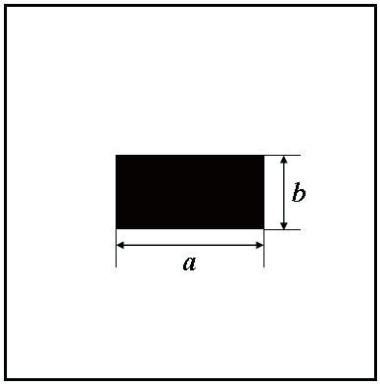


Figure 16: Porosity effect using a rectangular solid.

https://doi.org/10.4208/cicp.210815.240316a Published online by Cambridge University Press

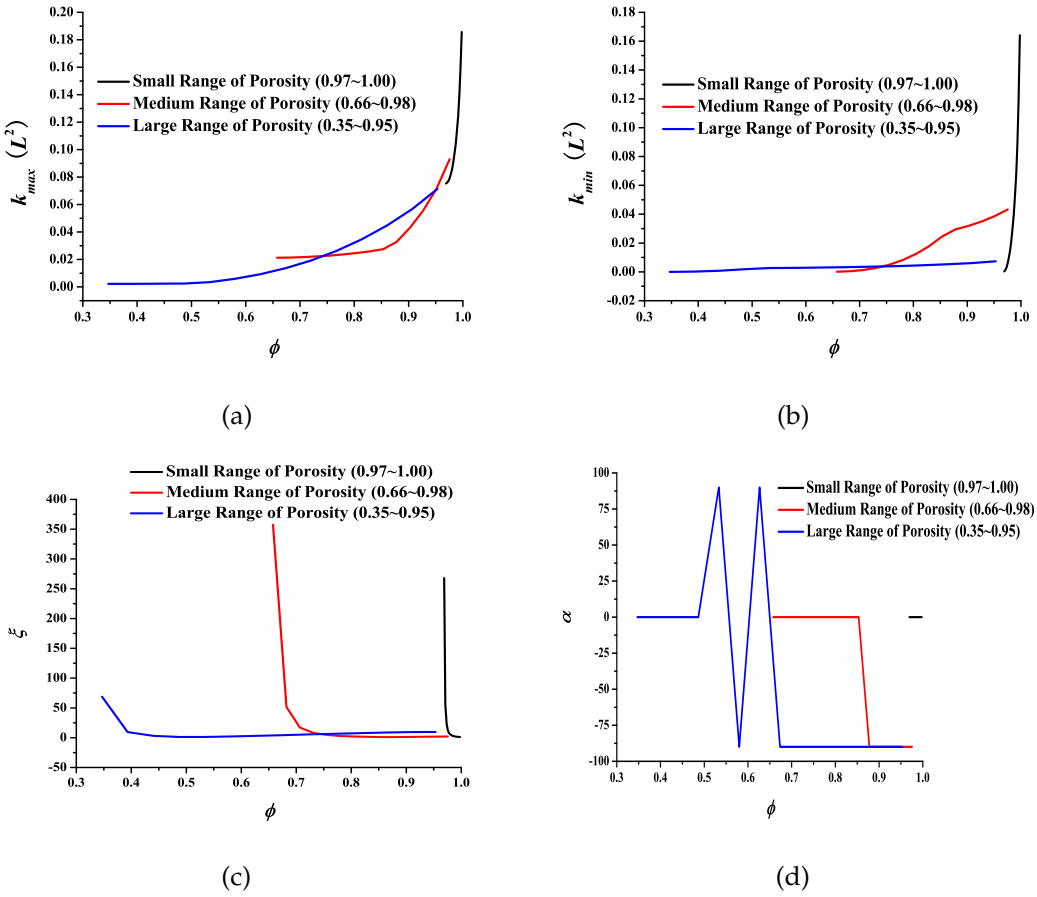


Figure 17: Results for different porosities using a rectangular solid: (a) maximum permeability; (b) minimum permeability; (c) anisotropic ratio; (d) principal direction.

The two sets of examples indicate that the relation between permeability and porosity for isotropic conditions is monotonic. However, their relation becomes much more complex for anisotropic conditions so that a general function relating the full-tensor permeability with porosity cannot be found. Thus, an accurate way to determine the permeability is our high accurate methods.

3.4 Effect of side length ratio

As shown in Fig. 16, the side length ratio of a solid is defined as:

$$\varepsilon = \frac{b}{a}. \tag{3.2}$$

Due to the limitation of the rectangular mesh in this study, the side lengths take the following values: $a = (36/60)L$, $(18/60)L$, $(12/60)L$, $(9/60)L$, $(8/60)L$, $(6/60)L$, $(4/60)L$,

https://doi.org/10.4208/cicp.210815.240316a Published online by Cambridge University Press

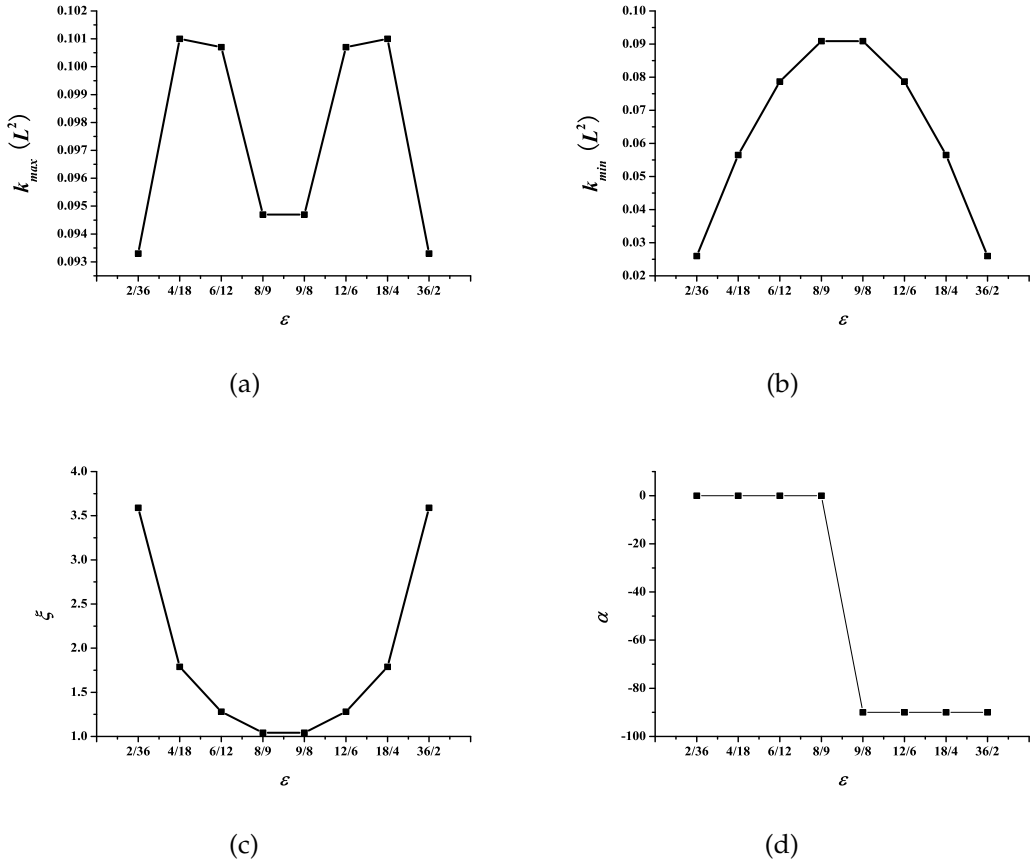


Figure 18: Results for different length ratio: (a) maximum permeability; (b) minimum permeability; (c) anisotropic ratio; (d) principal direction.

$(2/60)L$; b=$(2/60)L$, $(4/60)L$, $(6/60)L$, $(8/60)L$, $(9/60)L$, $(12/60)L$, $(18/60)L$, $(36/60)L$. Thus, the corresponding ε is: 2/36, 4/18, 6/12, 8/9, 9/8, 12/6, 18/4, 36/2. According to Eq. (3.1), the porosities of all these ε are same ($\phi=0.98$) so that the effect of side length ratio is studied at the constant porosity. Fig. 18 shows that $k_{\max}$, $k_{\min}$ and ξ distribute symmetrically around $\varepsilon=1$, but $\alpha=0^\circ$ for $\varepsilon<1$ and $\alpha=-90^\circ$ for $\varepsilon>1$. This demonstrates that the orientation of the solid does not change the value of permeability and anisotropy but only changes the principal direction.

3.5 Benchmark solutions of full-tensor and effective permeability

From the analyses in Sections 3.2-3.5, it is hard to establish a general model to describe the relations of the full-tensor permeability with the porosity and the side length ratio of solids. On the other hand, computation for a single case using our high accurate meth-

https://doi.org/10.4208/cicp.210815.240316a Published online by Cambridge University Press

ods is very fast (within 10 seconds). Therefore, an efficient way to obtain high-accurate full-tensor permeability and corresponding effective permeability is the newly proposed methods in this study. As discussed in Section 2, the results obtained by this method are high-accurate and grid independent. Thus, they can be considered as benchmark solutions. With this efficient method, we can master the characteristics of reservoirs with any shape of complex structures on rectangular mesh and provide key parameters for reservoir simulations. Among of them, 90 typical structures are selected to be shown in Appendix B.

Cases 1-4 are structures with different-dimension single solids. All of them show isotropy and decreasing permeability with increasing dimension of the solid. Cases 5-12 are double-solids systems. Most of them show weak anisotropy and the principal directions are the same as the orientations of the solids. However, isotropy appears when the distance between the two solids achieves $(4/10)L$ (Case 9 and Case 10). This is because this distance can produce a symmetric structure in the condition of periodic boundaries. Cases 13-18 are connected-solids systems on the diagonal or off-diagonal lines of the domain. They show much stronger anisotropy than Cases 5-12. The anisotropic ratio becomes larger with larger dimension of the system. The principal directions are also the same as the orientations of the solids. Cases 19-27 are symmetric systems containing different numbers and different shapes of solids. They all show isotropy. Cases 28-33 are structures with single large rectangular solid. The anisotropy is only related to the length of the solid while the principal directions are always along the longer side of the rectangular solid. Once the same-dimensional rectangular solids with different orientations are combined, they show isotropy again (Cases 34-35). Cases 36-69 are systematic and quantitative studies on anisotropic structures. It can be seen that slight variations of the solids cause apparent variations of anisotropy and principal direction. Cases 70-90 are some interesting or randomly distributed structures.

4 Conclusions

A steady-state Stokes flow is used as an approach for numerically determining the full-tensor permeability by connecting continuum scale and Darcy scale. A high-accurate finite difference method is designed for obtaining high-accurate velocity fields of the Stokes flows. Then, a high-accurate numerical integration method is designed for obtaining high-accurate mean velocity to determine the full-tensor permeability precisely. The high-accurate finite difference method should match the high-accurate numerical integration method. Otherwise, the accuracy may be lost severely so that the effort on constructing the high-accurate finite difference method becomes meaningless. This principle can be a general guideline for the numerical applications needing extreme high accuracy.

By using the high-accurate methods and applying the eigenvalue problems, important parameters such as the maximum and minimum permeabilities, principal directions and anisotropies are calculated. Relations of these parameters with solid position, poros-

https://doi.org/10.4208/cicp.210815.240316a Published online by Cambridge University Press

ity and side length ratio of solids are discussed. The results show that the position of solids does not affect these parameters. However, other relations are so complicated that no model can be established to reveal them properly. Therefore, the efficient way to predict these parameters is the high-accurate methods proposed in this study.

Full-tensor permeability and the above four parameters are calculated for as many as 90 structures of porous media as benchmark solutions. These structures include symmetric or non-symmetric structures, ensemble or scattered structures. Anisotropic ratios in the range of 1.0000-23.6212 and principal directions in the range of −90-90 are detected. The results are valuable reference for complex reservoir simulations.

Acknowledgments

The work presented in this paper has been supported in part by the project entitled "Simulation of Subsurface Geochemical Transport and Carbon Sequestration", funded by the GRP-AEA Program at KAUST and also supported by National Science Foundation of China (No.51576210, No.51206186), and Science Foundation of China University of Petroleum-Beijing (No.2462015BJB03, No.2462015YQ0409).

Appendix A: Derivation of the high-order sub-domain integration

For $N=1$:

Only 1 quadratic polynomial need to be constructed as shown in Fig. 19 so that it satisfies:

$$\begin{cases} ax_0^2+bx_0+c=v_0, \\ ax_1^2+bx_1+c=v_1, \\ ax_2^2+bx_2+c=v_2, \end{cases} \tag{A.1}$$

where

$$x_1-x_0=x_2-x_1=\Delta x/2, \qquad x_2-x_0=\Delta x.$$

Solve Eq. (A.1) and we can obtain:

$$\begin{aligned} a&=\frac{2}{(\Delta x)^2}(v_0-2v_1+v_2), \\ b&=\frac{2}{(\Delta x)^2}[-(x_2+x_1)v_0+(x_2+2x_1+x_0)v_1-(x_1+x_0)v_2], \\ c&=\frac{2}{(\Delta x)^2}(x_1x_2v_0-2x_0x_2v_1+x_0x_1v_2). \end{aligned} \tag{A.2}$$

https://doi.org/10.4208/cicp.210815.240316a Published online by Cambridge University Press

Thus, the integration is:

$$\begin{aligned}
\int_V v dV &= \int_{x_1-\Delta x/2}^{x_1+\Delta x/2} \left(ax^2+bx+c\right) dx = \frac{1}{3}ax^3+\frac{1}{2}bx^2+cx\Big|_{x_1-\Delta x/2}^{x_1+\Delta x/2} \\
&= \frac{1}{3}a\left[\left(x_1+\frac{\Delta x}{2}\right)^3-\left(x_1-\frac{\Delta x}{2}\right)^3\right]+\frac{1}{2}b\left[\left(x_1+\frac{\Delta x}{2}\right)^2-\left(x_1-\frac{\Delta x}{2}\right)^2\right]+c\Delta x \\
&= \frac{1}{3}a\left[3(x_1)^2\Delta x+\frac{(\Delta x)^3}{4}\right]+\frac{1}{2}b2x_1\Delta x+c\Delta x \\
&= a\left[(x_1)^2\Delta x+\frac{(\Delta x)^3}{12}\right]+bx_1\Delta x+c\Delta x \\
&= \Delta x\left\{\begin{array}{l}
\dfrac{2}{(\Delta x)^2}(v_0-2v_1+v_2)\left[(x_1)^2+\dfrac{(\Delta x)^2}{12}\right] \\
+\dfrac{2}{(\Delta x)^2}\left[-(x_2+x_1)v_0+(x_2+2x_1+x_0)v_1-(x_1+x_0)v_2\right]x_1 \\
+\dfrac{2}{(\Delta x)^2}(x_1x_2v_0-2x_0x_2v_1+x_0x_1v_2)
\end{array}\right\} \\
&= \Delta x\frac{2}{(\Delta x)^2}\left\{\begin{array}{l}
(v_0-2v_1+v_2)\left[(x_1)^2+\dfrac{(\Delta x)^2}{12}\right] \\
+\left[-(x_2+x_1)v_0+(x_2+2x_1+x_0)v_1-(x_1+x_0)v_2\right]x_1 \\
+(x_1x_2v_0-2x_0x_2v_1+x_0x_1v_2)
\end{array}\right\} \\
&= \frac{2}{\Delta x}\left\{\frac{(\Delta x)^2}{12}v_0+\left[-\frac{(\Delta x)^2}{6}+x_1x_2+x_0x_1-2x_0x_2\right]v_1+\frac{(\Delta x)^2}{12}v_2\right\},
\end{aligned} \tag{A.3}$$

where

$$x_1x_2+x_0x_1-2x_0x_2 = x_2(x_1-x_0)+x_0(x_1-x_2) = x_2\frac{\Delta x}{2}-x_0\frac{\Delta x}{2} = \frac{(\Delta x)^2}{2}.$$

Thus,

$$\begin{aligned}
\int_V v dV &= \frac{2}{\Delta x}\left\{\frac{(\Delta x)^2}{12}v_0+\left[-\frac{(\Delta x)^2}{6}+\frac{(\Delta x)^2}{2}\right]v_1+\frac{(\Delta x)^2}{12}v_2\right\} \\
&= \Delta x\left(\frac{1}{6}v_0+\frac{2}{3}v_1+\frac{1}{6}v_2\right).
\end{aligned} \tag{A.4}$$

https://doi.org/10.4208/cicp.210815.240316a Published online by Cambridge University Press

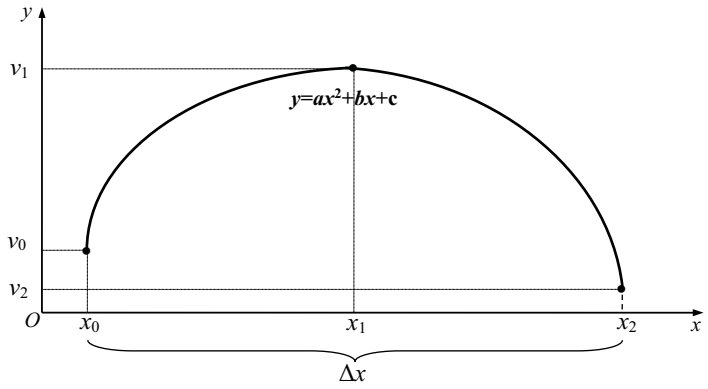


Figure 19: High-order sub-domain integration for $N=1$.

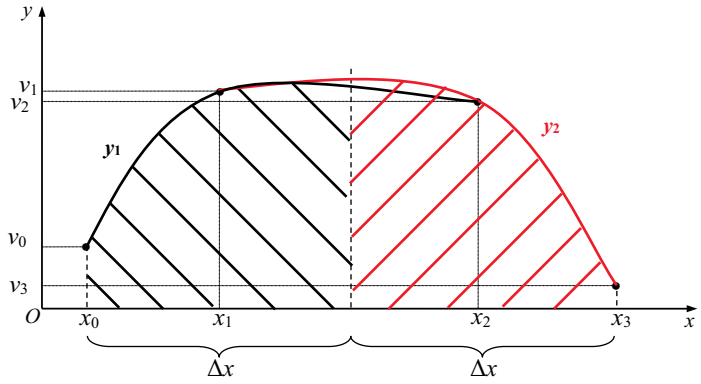


Figure 20: High-order sub-domain integration for $N=2$.

For $N=2$:

Two quadratic polynomials need to be constructed as shown in Fig. 20 so that:

$$\begin{cases} a_1x_0^2+b_1x_0+c_1=v_0, \\ a_1x_1^2+b_1x_1+c_1=v_1, \\ a_1x_2^2+b_1x_2+c_1=v_2, \end{cases} \quad \text{and} \quad \begin{cases} a_2x_1^2+b_2x_1+c_2=v_1, \\ a_2x_2^2+b_2x_2+c_2=v_2, \\ a_2x_3^2+b_2x_3+c_2=v_3, \end{cases} \tag{A.5}$$

where $x_1-x_0=x_3-x_2=\Delta x/2$, $x_2-x_1=\Delta x$. Solve Eq. (A.5) and we can obtain:

$$a_1=\frac{2}{3(\Delta x)^2}(2v_0-3v_1+v_2), \tag{A.6}$$

$$b_1=\frac{2}{3(\Delta x)^2}[-2(x_2+x_1)v_0+(2x_2+3x_1+x_0)v_1-(x_1+x_0)v_2], \tag{A.7}$$

https://doi.org/10.4208/cicp.210815.240316a Published online by Cambridge University Press

$$c_1=\frac{2}{3(\Delta x)^2}(2x_1x_2v_0-3x_0x_2v_1+x_0x_1v_2), \tag{A.8}$$

$$a_2=\frac{2}{3(\Delta x)^2}(v_1-3v_2+2v_3), \tag{A.9}$$

$$b_2=\frac{2}{3(\Delta x)^2}[-(x_3+x_2)v_1+(x_3+3x_2+2x_1)v_2-2(x_2+x_1)v_3], \tag{A.10}$$

$$c_2=\frac{2}{3(\Delta x)^2}(x_2x_3v_1-3x_1x_3v_2+2x_1x_2v_3). \tag{A.11}$$

Do the similar integration of Eq. (A.3)-Eq. (A.4), we can obtain:

$$\begin{aligned}\int_V vdV&=\int_{x_1-\Delta x/2}^{x_1+\Delta x/2}(a_1x^2+b_1x+c_1)dx+\int_{x_2-\Delta x/2}^{x_2+\Delta x/2}(a_2x^2+b_2x+c_2)dx\\&=\Delta x\left(\frac{1}{9}v_0+\frac{5}{6}v_1+\frac{1}{18}v_2\right)+\Delta x\left(\frac{1}{18}v_1+\frac{5}{6}v_2+\frac{1}{9}v_3\right)\\&=\Delta x\left(\frac{1}{9}v_0+\frac{8}{9}v_1+\frac{8}{9}v_2+\frac{1}{9}v_3\right).\end{aligned} \tag{A.12}$$

For $N=3$:

The derivation is completely similar with the derivation of $N=1$ and $N=2$. The final expression is:

$$\begin{aligned}\int_V vdV&=\int_{x_1-\Delta x/2}^{x_1+\Delta x/2}(a_1x^2+b_1x+c_1)dx+\int_{x_2-\Delta x/2}^{x_2+\Delta x/2}(a_2x^2+b_2x+c_2)dx\\&\quad+\int_{x_3-\Delta x/2}^{x_3+\Delta x/2}(a_3x^2+b_3x+c_3)dx\\&=\Delta x\left(\frac{1}{9}v_0+\frac{5}{6}v_1+\frac{1}{18}v_2\right)+\Delta x\left(\frac{1}{24}v_1+\frac{11}{12}v_2+\frac{1}{24}v_3\right)+\Delta x\left(\frac{1}{18}v_2+\frac{5}{6}v_3+\frac{1}{9}v_4\right)\\&=\Delta x\left(\frac{1}{9}v_0+\frac{7}{8}v_1+\frac{37}{36}v_2+\frac{7}{8}v_3+\frac{1}{9}v_4\right).\end{aligned} \tag{A.13}$$

For $N=4$:

$$\begin{aligned}\int_V vdV&=\int_{x_1-\Delta x/2}^{x_1+\Delta x/2}(a_1x^2+b_1x+c_1)dx+\int_{x_2-\Delta x/2}^{x_2+\Delta x/2}(a_2x^2+b_2x+c_2)dx\\&\quad+\int_{x_3-\Delta x/2}^{x_3+\Delta x/2}(a_3x^2+b_3x+c_3)dx+\int_{x_4-\Delta x/2}^{x_4+\Delta x/2}(a_4x^2+b_4x+c_4)dx\\&=\Delta x\left(\frac{1}{9}v_0+\frac{5}{6}v_1+\frac{1}{18}v_2\right)+\Delta x\left(\frac{1}{24}v_1+\frac{11}{12}v_2+\frac{1}{24}v_3\right)\\&\quad+\Delta x\left(\frac{1}{24}v_2+\frac{11}{12}v_3+\frac{1}{24}v_4\right)+\Delta x\left(\frac{1}{18}v_3+\frac{5}{6}v_4+\frac{1}{9}v_5\right)\end{aligned}$$

https://doi.org/10.4208/cicp.210815.240316a Published online by Cambridge University Press

$$=\Delta x\left(\frac{1}{9}v_0+\frac{7}{8}v_1+\frac{73}{72}v_2+\frac{73}{72}v_3+\frac{7}{8}v_4+\frac{1}{9}v_5\right). \tag{A.14}$$

For $N=5$:

$$\int_V vdV=\Delta x\left(\frac{1}{9}v_0+\frac{7}{8}v_1+\frac{73}{72}v_2+v_3+\frac{73}{72}v_4+\frac{7}{8}v_5+\frac{1}{9}v_6\right). \tag{A.15}$$

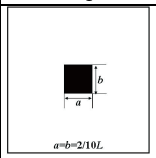
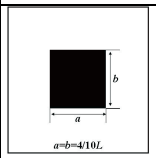
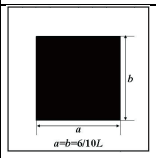
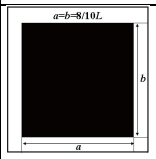
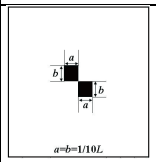
For $N>5$:

It can be expected from the above derivation and Fig. 6 that the coefficients of $v_3,\cdots,v_{n-2}$ are all 1 so that:

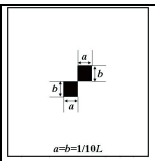
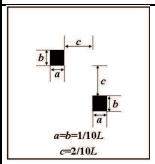
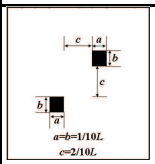
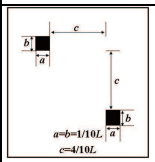
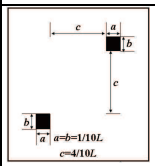
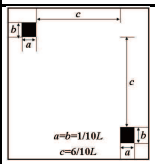
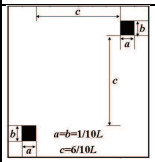
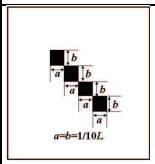
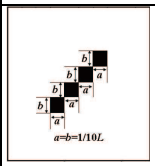
$$\int_V vdV=\Delta x\left(\frac{1}{9}v_0+\frac{7}{8}v_1+\frac{73}{72}v_2+v_3+\cdots v_{n-2}+\frac{73}{72}v_{n-1}+\frac{7}{8}v_n+\frac{1}{9}v_{n+1}\right). \tag{A.16}$$

Summarize Eq. (A.4), Eq. (A.12)-Eq. (A.16), we can obtain the expression of Eq. (2.29).

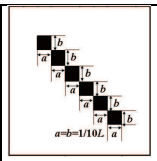
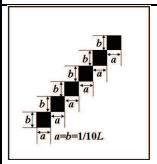
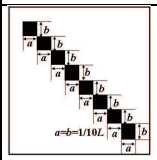
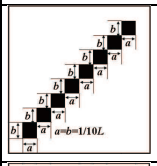
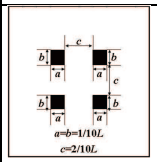
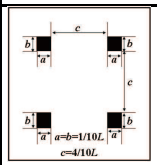
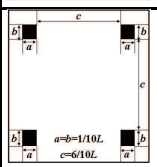
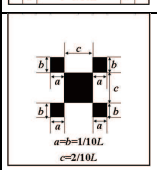
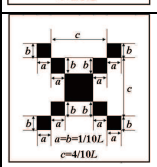
Appendix B: Full-tensor permeability and related parameters for various reservoir structures

Case Number	Case Description	$\mathbf{k}(\times L^2)$	$\mathbf{k}_{eff}(\times L^2)$	α	ξ
1		$\begin{bmatrix} 0.0675 & 0.0000 \\ 0.0000 & 0.0675 \end{bmatrix}$	$\begin{bmatrix} 0.0675 & 0.0000 \\ 0.0000 & 0.0675 \end{bmatrix}$	N/A	1.0000
2		$\begin{bmatrix} 0.0237 & 0.0000 \\ 0.0000 & 0.0237 \end{bmatrix}$	$\begin{bmatrix} 0.0237 & 0.0000 \\ 0.0000 & 0.0237 \end{bmatrix}$	N/A	1.0000
3		$\begin{bmatrix} 0.0064 & 0.0000 \\ 0.0000 & 0.0064 \end{bmatrix}$	$\begin{bmatrix} 0.0064 & 0.0000 \\ 0.0000 & 0.0064 \end{bmatrix}$	N/A	1.0000
4		$\begin{bmatrix} 7.2530\times10^{-4} & 0.0000 \\ 0.0000 & 7.2530\times10^{-4} \end{bmatrix}$	$\begin{bmatrix} 7.2530\times10^{-4} & 0.0000 \\ 0.0000 & 7.2530\times10^{-4} \end{bmatrix}$	N/A	1.0000
5		$\begin{bmatrix} 0.0798 & -0.0109 \\ -0.0109 & 0.0798 \end{bmatrix}$	$\begin{bmatrix} 0.0908 & 0.0000 \\ 0.0000 & 0.0689 \end{bmatrix}$	-45°	1.3172

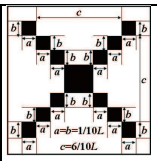
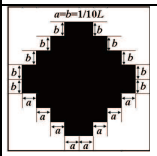
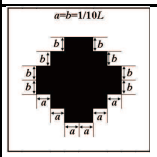
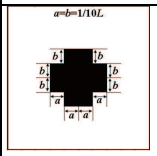
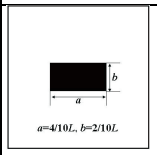
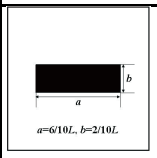
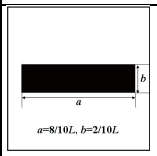
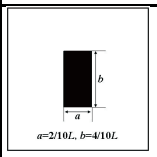
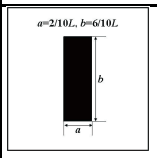
https://doi.org/10.4208/cicp.210815.240316a Published online by Cambridge University Press

6		$\begin{bmatrix} 0.0798 & 0.0109 \\ 0.0109 & 0.0000 \end{bmatrix}$	$\begin{bmatrix} 0.0908 & 0.0000 \\ 0.0000 & 0.0689 \end{bmatrix}$	45°	1.3172
7		$\begin{bmatrix} 0.0512 & -0.0068 \\ -0.0068 & 0.0512 \end{bmatrix}$	$\begin{bmatrix} 0.0580 & 0.0000 \\ 0.0000 & 0.0444 \end{bmatrix}$	−45°	1.3058
8		$\begin{bmatrix} 0.0512 & 0.0068 \\ 0.0068 & 0.0512 \end{bmatrix}$	$\begin{bmatrix} 0.0580 & 0.0000 \\ 0.0000 & 0.0444 \end{bmatrix}$	45°	1.3058
9		$\begin{bmatrix} 0.00460 & 0.0000 \\ 0.0000 & 0.0460 \end{bmatrix}$	$\begin{bmatrix} 0.00460 & 0.0000 \\ 0.0000 & 0.0460 \end{bmatrix}$	N/A	1.0000
10		$\begin{bmatrix} 0.00460 & 0.0000 \\ 0.0000 & 0.0460 \end{bmatrix}$	$\begin{bmatrix} 0.00460 & 0.0000 \\ 0.0000 & 0.0460 \end{bmatrix}$	N/A	1.0000
11		$\begin{bmatrix} 0.0512 & -0.0068 \\ -0.0068 & 0.0512 \end{bmatrix}$	$\begin{bmatrix} 0.0580 & 0.0000 \\ 0.0000 & 0.0444 \end{bmatrix}$	−45°	1.3058
12		$\begin{bmatrix} 0.0512 & 0.0068 \\ 0.0068 & 0.0512 \end{bmatrix}$	$\begin{bmatrix} 0.0580 & 0.0000 \\ 0.0000 & 0.0444 \end{bmatrix}$	45°	1.3058
13		$\begin{bmatrix} 0.0413 & -0.0133 \\ -0.0133 & 0.0413 \end{bmatrix}$	$\begin{bmatrix} 0.0546 & 0.0000 \\ 0.0000 & 0.0281 \end{bmatrix}$	−45°	1.9441
14		$\begin{bmatrix} 0.0413 & 0.0133 \\ 0.0133 & 0.0413 \end{bmatrix}$	$\begin{bmatrix} 0.0546 & 0.0000 \\ 0.0000 & 0.0281 \end{bmatrix}$	45°	1.9441

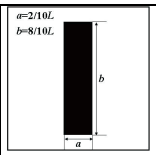
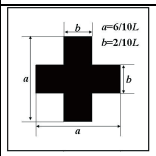
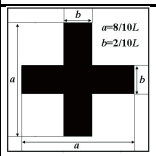
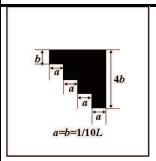
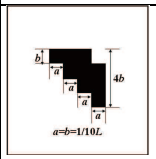
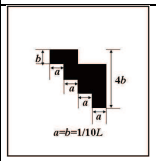
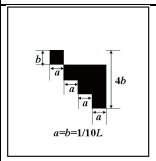
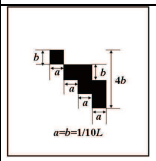
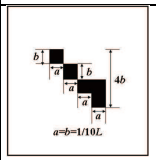
https://doi.org/10.4208/cicp.210815.240316a Published online by Cambridge University Press

15		$\begin{bmatrix} 0.0232 & -0.0113 \\ -0.0113 & 0.0232 \end{bmatrix}$	$\begin{bmatrix} 0.0345 & 0.0000 \\ 0.0000 & 0.0119 \end{bmatrix}$	-45°	2.8896
16		$\begin{bmatrix} 0.0232 & 0.0113 \\ 0.0113 & 0.0232 \end{bmatrix}$	$\begin{bmatrix} 0.0345 & 0.0000 \\ 0.0000 & 0.0119 \end{bmatrix}$	45°	2.8896
17		$\begin{bmatrix} 0.0148 & -0.0114 \\ -0.0114 & 0.0148 \end{bmatrix}$	$\begin{bmatrix} 0.0261 & 0.0000 \\ 0.0000 & 0.0034 \end{bmatrix}$	-45°	7.7267
18		$\begin{bmatrix} 0.0148 & 0.0114 \\ 0.0114 & 0.0148 \end{bmatrix}$	$\begin{bmatrix} 0.0261 & 0.0000 \\ 0.0000 & 0.0034 \end{bmatrix}$	45°	7.7267
19		$\begin{bmatrix} 0.0270 & 0.0000 \\ 0.0000 & 0.0270 \end{bmatrix}$	$\begin{bmatrix} 0.0270 & 0.0000 \\ 0.0000 & 0.0270 \end{bmatrix}$	N/A	1.0000
20		$\begin{bmatrix} 0.0169 & 0.0000 \\ 0.0000 & 0.0169 \end{bmatrix}$	$\begin{bmatrix} 0.0169 & 0.0000 \\ 0.0000 & 0.0169 \end{bmatrix}$	N/A	1.0000
21		$\begin{bmatrix} 0.0270 & 0.0000 \\ 0.0000 & 0.0270 \end{bmatrix}$	$\begin{bmatrix} 0.0270 & 0.0000 \\ 0.0000 & 0.0270 \end{bmatrix}$	N/A	1.0000
22		$\begin{bmatrix} 0.0246 & 0.0000 \\ 0.0000 & 0.0246 \end{bmatrix}$	$\begin{bmatrix} 0.0246 & 0.0000 \\ 0.0000 & 0.0246 \end{bmatrix}$	N/A	1.0000
23		$\begin{bmatrix} 0.0278 & 0.0000 \\ 0.0000 & 0.0278 \end{bmatrix}$	$\begin{bmatrix} 0.0278 & 0.0000 \\ 0.0000 & 0.0278 \end{bmatrix}$	N/A	1.0000

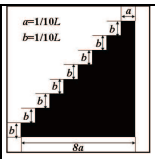
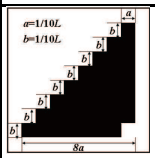
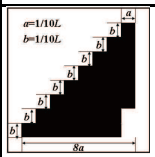
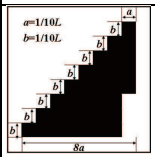
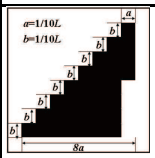
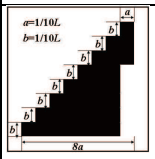
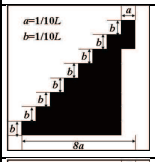
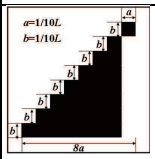
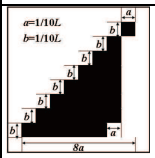
https://doi.org/10.4208/cicp.210815.240316a Published online by Cambridge University Press

24		$\begin{bmatrix} 0.0014 & 0.0000 \\ 0.0000 & 0.0014 \end{bmatrix}$	$\begin{bmatrix} 0.0014 & 0.0000 \\ 0.0000 & 0.0014 \end{bmatrix}$	N/A	1.0000
25		$\begin{bmatrix} 0.0018 & 0.0000 \\ 0.0000 & 0.0018 \end{bmatrix}$	$\begin{bmatrix} 0.0018 & 0.0000 \\ 0.0000 & 0.0018 \end{bmatrix}$	N/A	1.0000
26		$\begin{bmatrix} 0.0105 & 0.0000 \\ 0.0000 & 0.0105 \end{bmatrix}$	$\begin{bmatrix} 0.0105 & 0.0000 \\ 0.0000 & 0.0105 \end{bmatrix}$	N/A	1.0000
27		$\begin{bmatrix} 0.0298 & 0.0000 \\ 0.0000 & 0.0298 \end{bmatrix}$	$\begin{bmatrix} 0.0298 & 0.0000 \\ 0.0000 & 0.0298 \end{bmatrix}$	N/A	1.0000
28		$\begin{bmatrix} 0.0537 & 0.0000 \\ 0.0000 & 0.0302 \end{bmatrix}$	$\begin{bmatrix} 0.0537 & 0.0000 \\ 0.0000 & 0.0302 \end{bmatrix}$	0°	1.7787
29		$\begin{bmatrix} 0.0467 & 0.0000 \\ 0.0000 & 0.0107 \end{bmatrix}$	$\begin{bmatrix} 0.0537 & 0.0000 \\ 0.0000 & 0.0302 \end{bmatrix}$	0°	4.3596
30		$\begin{bmatrix} 0.0436 & 0.0000 \\ 0.0000 & 0.0018 \end{bmatrix}$	$\begin{bmatrix} 0.0436 & 0.0000 \\ 0.0000 & 0.0018 \end{bmatrix}$	0°	23.6212
31		$\begin{bmatrix} 0.0302 & 0.0000 \\ 0.0000 & 0.0537 \end{bmatrix}$	$\begin{bmatrix} 0.0537 & 0.0000 \\ 0.0000 & 0.0302 \end{bmatrix}$	−90°	1.7787
32		$\begin{bmatrix} 0.0107 & 0.0000 \\ 0.0000 & 0.0467 \end{bmatrix}$	$\begin{bmatrix} 0.0467 & 0.0000 \\ 0.0000 & 0.0107 \end{bmatrix}$	−90°	4.3596

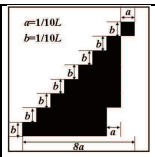
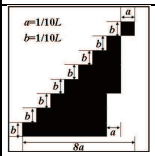
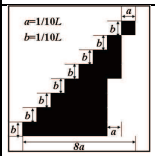
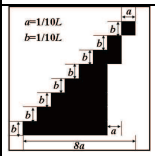
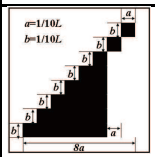
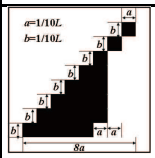
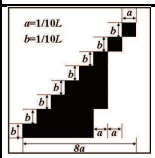
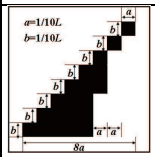
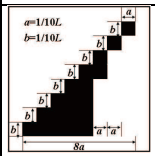
https://doi.org/10.4208/cicp.210815.240316a Published online by Cambridge University Press

33		$\begin{bmatrix} 0.0018 & 0.0000 \\ 0.0000 & 0.0436 \end{bmatrix}$	$\begin{bmatrix} 0.0436 & 0.0000 \\ 0.0000 & 0.0018 \end{bmatrix}$	90°	23.6212
34		$\begin{bmatrix} 0.0106 & 0.0000 \\ 0.0000 & 0.0106 \end{bmatrix}$	$\begin{bmatrix} 0.0106 & 0.0000 \\ 0.0000 & 0.0106 \end{bmatrix}$	N/A	1.0000
35		$\begin{bmatrix} 0.0018 & 0.0000 \\ 0.0000 & 0.0018 \end{bmatrix}$	$\begin{bmatrix} 0.0018 & 0.0000 \\ 0.0000 & 0.0018 \end{bmatrix}$	N/A	1.0000
36		$\begin{bmatrix} 0.0299 & -0.0041 \\ -0.0041 & 0.0299 \end{bmatrix}$	$\begin{bmatrix} 0.0340 & 0.0000 \\ 0.0000 & 0.0259 \end{bmatrix}$	−45°	1.3150
37		$\begin{bmatrix} 0.0324 & -0.0062 \\ -0.0062 & 0.0324 \end{bmatrix}$	$\begin{bmatrix} 0.0386 & 0.0000 \\ 0.0000 & 0.0262 \end{bmatrix}$	−45°	1.4768
38		$\begin{bmatrix} 0.0347 & -0.0071 \\ -0.007 & 0.0327 \end{bmatrix}$	$\begin{bmatrix} 0.0409 & 0.0000 \\ 0.0000 & 0.0266 \end{bmatrix}$	−41.11°	1.5386
39		$\begin{bmatrix} 0.0368 & -0.0076 \\ -0.0076 & 0.0329 \end{bmatrix}$	$\begin{bmatrix} 0.0427 & 0.0000 \\ 0.0000 & 0.0270 \end{bmatrix}$	−37.74°	1.5824
40		$\begin{bmatrix} 0.0389 & -0.0102 \\ -0.0101 & 0.0364 \end{bmatrix}$	$\begin{bmatrix} 0.0479 & 0.0000 \\ 0.0000 & 0.0274 \end{bmatrix}$	−41.56°	1.7452
41		$\begin{bmatrix} 0.0400 & -0.0109 \\ -0.0109 & 0.0369 \end{bmatrix}$	$\begin{bmatrix} 0.0495 & 0.0000 \\ 0.0000 & 0.0275 \end{bmatrix}$	−41.00°	1.8002

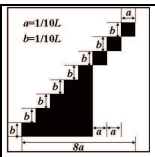
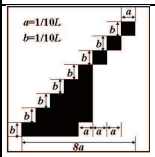
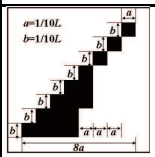
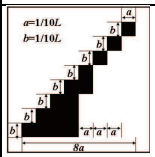
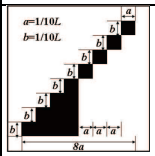
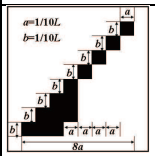
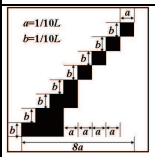
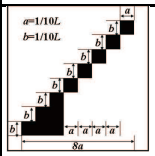
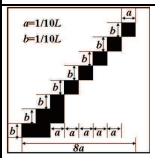
https://doi.org/10.4208/cicp.210815.240316a Published online by Cambridge University Press

42		$\begin{bmatrix} 0.0020 & 0.0002 \\ 0.0002 & 0.0020 \end{bmatrix}$	$\begin{bmatrix} 0.0022 & 0.0000 \\ 0.0000 & 0.0017 \end{bmatrix}$	45°	1.2620
43		$\begin{bmatrix} 0.0023 & 0.0005 \\ 0.0005 & 0.0023 \end{bmatrix}$	$\begin{bmatrix} 0.0028 & 0.0000 \\ 0.0000 & 0.0019 \end{bmatrix}$	45°	1.5321
44		$\begin{bmatrix} 0.0024 & 0.0006 \\ 0.0006 & 0.0030 \end{bmatrix}$	$\begin{bmatrix} 0.0034 & 0.0000 \\ 0.0000 & 0.0020 \end{bmatrix}$	57.31°	1.7124
45		$\begin{bmatrix} 0.0024 & 0.0007 \\ 0.0007 & 0.0035 \end{bmatrix}$	$\begin{bmatrix} 0.0039 & 0.0000 \\ 0.0000 & 0.0020 \end{bmatrix}$	63.69°	1.9202
46		$\begin{bmatrix} 0.0024 & 0.0008 \\ 0.0008 & 0.0039 \end{bmatrix}$	$\begin{bmatrix} 0.0043 & 0.0000 \\ 0.0000 & 0.0021 \end{bmatrix}$	66.22°	2.0731
47		$\begin{bmatrix} 0.0024 & 0.0009 \\ 0.0009 & 0.0041 \end{bmatrix}$	$\begin{bmatrix} 0.0045 & 0.0000 \\ 0.0000 & 0.0021 \end{bmatrix}$	67.28°	2.1647
48		$\begin{bmatrix} 0.0024 & 0.0009 \\ 0.0009 & 0.0042 \end{bmatrix}$	$\begin{bmatrix} 0.0046 & 0.0000 \\ 0.0000 & 0.0021 \end{bmatrix}$	67.80°	2.2184
49		$\begin{bmatrix} 0.0024 & 0.0009 \\ 0.0009 & 0.0043 \end{bmatrix}$	$\begin{bmatrix} 0.0047 & 0.0000 \\ 0.0000 & 0.0021 \end{bmatrix}$	68.19°	2.2529
50		$\begin{bmatrix} 0.0033 & 0.0015 \\ 0.0015 & 0.0048 \end{bmatrix}$	$\begin{bmatrix} 0.0057 & 0.0000 \\ 0.0000 & 0.0024 \end{bmatrix}$	58.42°	2.3696

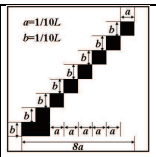
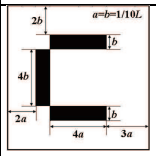
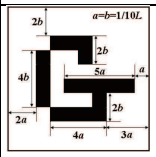
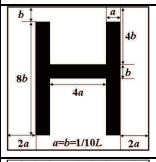
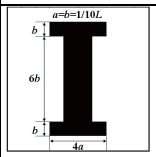
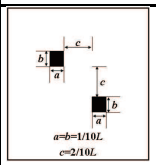
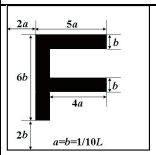
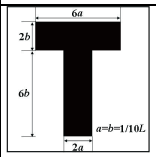
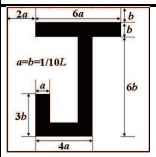
https://doi.org/10.4208/cicp.210815.240316a Published online by Cambridge University Press

51		$\begin{bmatrix} 0.0035 & 0.0017 \\ 0.0017 & 0.0053 \end{bmatrix}$	$\begin{bmatrix} 0.0064 & 0.0000 \\ 0.0000 & 0.0024 \end{bmatrix}$	59.16°	2.6423
52		$\begin{bmatrix} 0.0035 & 0.0019 \\ 0.0019 & 0.0058 \end{bmatrix}$	$\begin{bmatrix} 0.0069 & 0.0000 \\ 0.0000 & 0.0024 \end{bmatrix}$	60.69°	2.8417
53		$\begin{bmatrix} 0.0035 & 0.0020 \\ 0.0020 & 0.0062 \end{bmatrix}$	$\begin{bmatrix} 0.0073 & 0.0000 \\ 0.0000 & 0.0025 \end{bmatrix}$	61.73°	2.9850
54		$\begin{bmatrix} 0.0036 & 0.0021 \\ 0.0021 & 0.0065 \end{bmatrix}$	$\begin{bmatrix} 0.0076 & 0.0000 \\ 0.0000 & 0.0025 \end{bmatrix}$	62.29°	3.0774
55		$\begin{bmatrix} 0.0036 & 0.0021 \\ 0.0021 & 0.0066 \end{bmatrix}$	$\begin{bmatrix} 0.0077 & 0.0000 \\ 0.0000 & 0.0025 \end{bmatrix}$	62.51°	3.1245
56		$\begin{bmatrix} 0.0049 & 0.0031 \\ 0.0031 & 0.0073 \end{bmatrix}$	$\begin{bmatrix} 0.0094 & 0.0000 \\ 0.0000 & 0.0028 \end{bmatrix}$	55.50°	3.3619
57		$\begin{bmatrix} 0.0053 & 0.0035 \\ 0.0035 & 0.0078 \end{bmatrix}$	$\begin{bmatrix} 0.0102 & 0.0000 \\ 0.0000 & 0.0028 \end{bmatrix}$	54.91°	3.6348
58		$\begin{bmatrix} 0.0054 & 0.0037 \\ 0.0037 & 0.0082 \end{bmatrix}$	$\begin{bmatrix} 0.0107 & 0.0000 \\ 0.0000 & 0.0028 \end{bmatrix}$	55.30°	3.8124
59		$\begin{bmatrix} 0.0054 & 0.0038 \\ 0.0038 & 0.0085 \end{bmatrix}$	$\begin{bmatrix} 0.0111 & 0.0000 \\ 0.0000 & 0.0028 \end{bmatrix}$	55.72°	3.9253

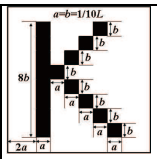
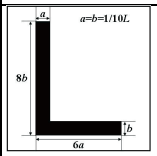
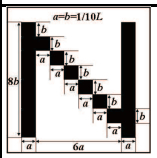
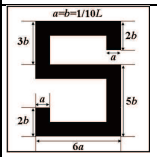
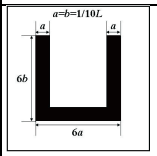
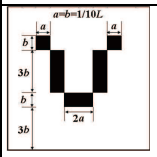
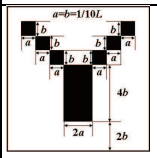
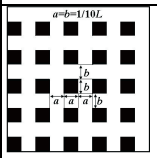
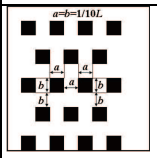
https://doi.org/10.4208/cicp.210815.240316a Published online by Cambridge University Press

60		$\begin{bmatrix} 0.0055 & 0.0039 \\ 0.0039 & 0.0086 \end{bmatrix}$	$\begin{bmatrix} 0.0113 & 0.0000 \\ 0.0000 & 0.0028 \end{bmatrix}$	55.96°	3.9848
61		$\begin{bmatrix} 0.0071 & 0.0052 \\ 0.0052 & 0.0096 \end{bmatrix}$	$\begin{bmatrix} 0.0137 & 0.0000 \\ 0.0000 & 0.0031 \end{bmatrix}$	51.62°	4.4800
62		$\begin{bmatrix} 0.0077 & 0.0057 \\ 0.0057 & 0.0101 \end{bmatrix}$	$\begin{bmatrix} 0.0146 & 0.0000 \\ 0.0000 & 0.0031 \end{bmatrix}$	50.95°	4.7699
63		$\begin{bmatrix} 0.0079 & 0.0059 \\ 0.0059 & 0.0104 \end{bmatrix}$	$\begin{bmatrix} 0.0151 & 0.0000 \\ 0.0000 & 0.0031 \end{bmatrix}$	50.97°	4.9321
64		$\begin{bmatrix} 0.0079 & 0.0060 \\ 0.0060 & 0.0105 \end{bmatrix}$	$\begin{bmatrix} 0.0154 & 0.0000 \\ 0.0000 & 0.0031 \end{bmatrix}$	51.07°	5.0108
65		$\begin{bmatrix} 0.0098 & 0.0075 \\ 0.0075 & 0.0117 \end{bmatrix}$	$\begin{bmatrix} 0.0183 & 0.0000 \\ 0.0000 & 0.0032 \end{bmatrix}$	48.49°	5.7044
66		$\begin{bmatrix} 0.0105 & 0.0080 \\ 0.0080 & 0.0121 \end{bmatrix}$	$\begin{bmatrix} 0.0194 & 0.0000 \\ 0.0000 & 0.0032 \end{bmatrix}$	47.97°	6.0020
67		$\begin{bmatrix} 0.0107 & 0.0082 \\ 0.0082 & 0.0123 \end{bmatrix}$	$\begin{bmatrix} 0.0198 & 0.0000 \\ 0.0000 & 0.0032 \end{bmatrix}$	47.89°	6.1237
68		$\begin{bmatrix} 0.0126 & 0.0097 \\ 0.0097 & 0.0135 \end{bmatrix}$	$\begin{bmatrix} 0.0228 & 0.0000 \\ 0.0000 & 0.0033 \end{bmatrix}$	46.31°	6.8785

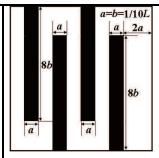
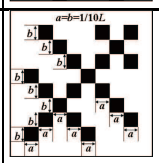
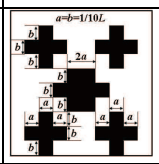
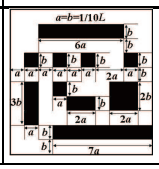
https://doi.org/10.4208/cicp.210815.240316a Published online by Cambridge University Press

69		$\begin{bmatrix} 0.0132 & 0.0102 \\ 0.0102 & 0.0138 \end{bmatrix}$	$\begin{bmatrix} 0.0237 & 0.0000 \\ 0.0000 & 0.0033 \end{bmatrix}$	45.98°	7.1256
70		$\begin{bmatrix} 0.0078 & 0.0000 \\ 0.0000 & 0.0145 \end{bmatrix}$	$\begin{bmatrix} 0.0145 & 0.0000 \\ 0.0000 & 0.0078 \end{bmatrix}$	$-90°$	1.8558
71		$\begin{bmatrix} 0.0085 & -0.0002 \\ -0.0002 & 0.0052 \end{bmatrix}$	$\begin{bmatrix} 0.0085 & 0.0000 \\ 0.0000 & 0.0052 \end{bmatrix}$	$-2.90°$	1.6285
72		$\begin{bmatrix} 0.0013 & 0.0000 \\ 0.0000 & 0.0056 \end{bmatrix}$	$\begin{bmatrix} 0.0056 & 0.0000 \\ 0.0000 & 0.0013 \end{bmatrix}$	$-90°$	4.1667
73		$\begin{bmatrix} 0.0012 & 0.0000 \\ 0.0000 & 0.0240 \end{bmatrix}$	$\begin{bmatrix} 0.0240 & 0.0000 \\ 0.0000 & 0.0012 \end{bmatrix}$	$-90°$	20.0411
74		$\begin{bmatrix} 0.0103 & 0.0010 \\ 0.0010 & 0.0137 \end{bmatrix}$	$\begin{bmatrix} 0.0140 & 0.0000 \\ 0.0000 & 0.0101 \end{bmatrix}$	75°	1.3840
75		$\begin{bmatrix} 0.0031 & 0.0000 \\ 0.0000 & 0.00117 \end{bmatrix}$	$\begin{bmatrix} 0.0117 & 0.0000 \\ 0.0000 & 0.0031 \end{bmatrix}$	90°	3.7299
76		$\begin{bmatrix} 0.0015 & 0.0000 \\ 0.0000 & 0.0105 \end{bmatrix}$	$\begin{bmatrix} 0.0105 & 0.0000 \\ 0.0000 & 0.0015 \end{bmatrix}$	90°	6.9415
77		$\begin{bmatrix} 0.0011 & 0.0002 \\ 0.0002 & 0.0102 \end{bmatrix}$	$\begin{bmatrix} 0.0102 & 0.0000 \\ 0.0000 & 0.0011 \end{bmatrix}$	88.54°	9.2097

https://doi.org/10.4208/cicp.210815.240316a Published online by Cambridge University Press

78		$\begin{bmatrix} 0.0014 & -0.0002 \\ -0.0002 & 0.0089 \end{bmatrix}$	$\begin{bmatrix} 0.0089 & 0.0000 \\ 0.0000 & 0.0014 \end{bmatrix}$	-88.56°	6.2490
79		$\begin{bmatrix} 0.0021 & -0.0006 \\ -0.0006 & 0.0100 \end{bmatrix}$	$\begin{bmatrix} 0.0101 & 0.0000 \\ 0.0000 & 0.0021 \end{bmatrix}$	-86.07°	4.7977
80		$\begin{bmatrix} 0.0014 & 0.0000 \\ 0.0000 & 0.0007 \end{bmatrix}$	$\begin{bmatrix} 0.0014 & 0.0000 \\ 0.0000 & 7.2540\times10^{-4} \end{bmatrix}$	0.0043°	1.9172
81		$\begin{bmatrix} 0.0009 & 0.0000 \\ 0.0000 & 0.0057 \end{bmatrix}$	$\begin{bmatrix} 0.0057 & 0.0000 \\ 0.0000 & 8.9050\times10^{-4} \end{bmatrix}$	89.98°	6.4483
82		$\begin{bmatrix} 0.0072 & 0.0000 \\ 0.0000 & 0.0064 \end{bmatrix}$	$\begin{bmatrix} 0.0072 & 0.0000 \\ 0.0000 & 0.0064 \end{bmatrix}$	0°	1.1263
83		$\begin{bmatrix} 0.0169 & 0.0000 \\ 0.0000 & 0.0119 \end{bmatrix}$	$\begin{bmatrix} 0.0169 & 0.0000 \\ 0.0000 & 0.0119 \end{bmatrix}$	0°	1.4198
84		$\begin{bmatrix} 0.0068 & 0.0000 \\ 0.0000 & 0.0025 \end{bmatrix}$	$\begin{bmatrix} 0.0068 & 0.0000 \\ 0.0000 & 0.0025 \end{bmatrix}$	0°	2.7031
85		$\begin{bmatrix} 5.2242\times10^{-4} & 0.0000 \\ 0.0000 & 5.2242\times10^{-4} \end{bmatrix}$	$\begin{bmatrix} 5.2242\times10^{-4} & 0.0000 \\ 0.0000 & 5.2242\times10^{-4} \end{bmatrix}$	N/A	1.0000
86		$\begin{bmatrix} 0.0008 & 0.0000 \\ 0.0000 & 0.0034 \end{bmatrix}$	$\begin{bmatrix} 0.0034 & 0.0000 \\ 0.0000 & 7.9931\times10^{-4} \end{bmatrix}$	-90°	4.2248

https://doi.org/10.4208/cicp.210815.240316a Published online by Cambridge University Press

87		$\begin{bmatrix} 0.0002 & 0.0000 \\ 0.0000 & 0.0027 \end{bmatrix}$	$\begin{bmatrix} 0.0027 & 0.0000 \\ 0.0000 & 2.2430\times10^{-4} \end{bmatrix}$	-89.72°	12.0779
88		$\begin{bmatrix} 0.0013 & 0.0001 \\ 0.0001 & 0.0013 \end{bmatrix}$	$\begin{bmatrix} 0.0014 & 0.0000 \\ 0.0000 & 0.0012 \end{bmatrix}$	45°	1.1868
89		$\begin{bmatrix} 0.0006 & 0.0000 \\ 0.0000 & 0.0016 \end{bmatrix}$	$\begin{bmatrix} 0.0016 & 0.0000 \\ 0.0000 & 5.5805\times10^{-4} \end{bmatrix}$	-90°	2.9141
90		$\begin{bmatrix} 0.0013 & 0.0001 \\ 0.0001 & 0.0007 \end{bmatrix}$	$\begin{bmatrix} 0.0013 & 0.0000 \\ 0.0000 & 7.0431\times10^{-4} \end{bmatrix}$	5.02°	1.8750

References

[1] Qiao, Z. and S. Sun (2014), Two-phase fluid simulation using a diffuse interface model with Peng-Robinson equation of state, SIAM J. Sci. Comput., 36(4), B708-B728.

[2] Dong, H., Z. Qiao, S. Sun, and T. Tang (2014), Adaptive moving grid methods for two-phase flow in porous media, J. Comput. Appl. Math., 265, 139-150.

[3] Kou, J. and S. Sun (2015), Numerical methods for a multi-component two-phase interface model with geometric mean influence parameters, SIAM J. Sci. Comput., 37(4), B543-B569.

[4] Kou, J. and S. Sun (2016), Unconditionally stable methods for simulating multi-component two-phase interface models with Peng-Robinson equation of state and various boundary conditions, J. Comput. Appl. Math., 291, 158-182.

[5] Darcy, H. (1856), Les Fontaines Publiques de la Vill de Dijon. Dalmont, Paris.

[6] Moortgat, J., S. Sun, and A. Firoozabadi (2011), Compositional modeling of three-phase flow with gravity using higher-order finite element methods, Water Resour. Res., 47, W05511.

[7] Sun, S. and J. Liu (2009), A locally conservative finite element method based on piecewise constant enrichment of the continuous Galerkin method, SIAM J. Sci. Comput., 31(4), 2528-2548.

[8] Sun, S. and M. F. Wheeler (2006a), Analysis of discontinuous Galerkin methods for multi-component reactive transport problems, Comput. Math. Appl., 52(5), 637-650.

[9] Sun, S. and M. F. Wheeler (2006b), A dynamic, adaptive, locally conservative and nonconforming solution strategy for transport phenomena in chemical engineering, Chem. Eng. Commun., 193(12), 1527-1545.

[10] Sun, S. and M. F. Wheeler (2007), Discontinuous Galerkin methods for simulating bioreactive transport of viruses in porous media, Adv. Water Resour., 30(6-7), 1696-1710.

[11] Hwang, W.R. and S.G. Advani (2010), Numerical simulations of Stokes-Brinkman equations for permeability prediction of dual scale fibrous porous media. Phys. Fluids, 22, 113101-1-14.

https://doi.org/10.4208/cicp.210815.240316a Published online by Cambridge University Press

[12] Jensen, J.L. and U. Heriot-Watt (1990), A model for small-scale permeability measurement with applications to reservoir characterization, paper presented at SPE/DOE Enhanced Oil Recovery Symposium, Society of Petroleum Engineers, Inc., Tulsa, Oklahoma.
[13] Wang, T.J., C.H. Wu, and L.J. Lee (1994), In-plane permeability measurement and analysis in liquid composite molding, Polym. Compos., 15(4), 278-288.
[14] Ferland, P., D. Guittard, and F. Trochu (1996), Concurrent methods for permeability measurement in resin transfer molding, Polym. Compos., 17(1), 149-158.
[15] Gauvin, R., F. Trochu, Y. Lemenn, and L. Diallo (1996), Permeability measurement and flow simulation through fiber reinforcement, Polym. Compos., 17(1), 34-42.
[16] Luo, Y., I. Verpoest, K. Hoes, M. Vanheule, H. Sol, and A. Cardon (2001), Permeability measurement of textile reinforcements with several test fluids, Composites Part A, 32(10), 1497-1504.
[17] Fwa, T.F., S.A. Tan, C.T. Chuai, and Y.K. Guwe (2001), Expedient permeability measurement for porous pavement surface. Int. J. Pavement Eng., 2(4), 259-270.
[18] Arbter, R., J.M. Beraud, C. Binetruy, L. Bizet, J. Brard, S. Comas-Cardona, C. Demaria, A. Endruweit, P. Ermanni, F. Gommer, S. Hasanovic, P. Henrat, F. Klunker, B. Laine, S. Lavanchy, S.V. Lomov, A. Long, V. Michaud, G. Morren, E. Ruiz, H. Sol, F. Trochu, B. Verleye, M. Wietgrefe, W. Wu, and G. Ziegmann (2011), Experimental determination of the permeability of textiles: A benchmark exercise, Composites Part A, 42(9), 1157-1168.
[19] Weitzenbock, J.R., R.A. Shenoi, and P.A. Wilson (1998), Measurement of principal permeability with the channel flow experiment, Polym. Compos., 20(2), 321-335.
[20] Weitzenbock, J.R., R.A. Shenoi, and P.A. Wilson (1999a), Radial flow permeability measurement. Part A: Theory, Composites Part A, 30(6), 781-796.
[21] Weitzenbock, J.R., R.A. Shenoi, and P.A. Wilson (1999b), Radial flow permeability measurement. Part B: Application, Composites Part A, 30(6), 797-813.
[22] Padmavathi, B.S., T. Amaranath, and S.D. Nigam (1993), Stokes flow past a porous sphere using Bringkman's model, Z. angew. Math. Phys., 44(5), 929-939.
[23] Ngo, N.D., and K.K. Tamma (2001), Microscale permeability predictions of porous fibrous media, Int. J. Heat Mass Transf., 44(16), 3135-3145.
[24] Al-Hadhrami, A.K., L. Elliott, and D.B. Ingham (2003), A new model for viscous dissipation in porous media across a range of permeability values, Transp. Porous Media, 53(1), 117-122.
[25] Ghaddar, C.K. (1995), On the permeability of unidirectional fibrous media: A parallel computational approach, Phys. Fluids, 7(11), 2563-2586.
[26] Wang, C.Y. (1996), Stokes flow through an array of rectangular fibers, Int. J. Multiph. Flow, 22(1), 185-194.
[27] Arbogast, T., and H.L. Lehr (2006), Homogenization of a Darcy-Stokes system modeling vuggy porous media, Comput. Geosci., 10(3), 291-302.
[28] Lemaitre, R., and P.M. Adler (1990), Fractal porous media IV: Three-dimensional Stokes flow through random media and rectangular fractals, Transp. Porous Media, 5(4), 325-340.
[29] Bosl, W.J. (1998), A study of porosity and permeability using a lattice Boltzmann simulation, Geophys. Res. Lett., 25(9), 1475-1478.
[30] Manwart, C., U. Aaltosalmi, A. Koponen, R. Hilfer, and J. Timonen (2002), Lattice-Boltzmann and finite-difference simulations for the permeability for three-dimensional porous media, Phys. Rev. E, 66(1), 016702-1-11.
[31] Li, X.Y. and B.E. Logan (2001), Permeability of fractal aggregates, Wat. Res., 35(14), 3373-3380.
[32] Zaman, Z. and J. Payman (2010), On hydraulic permeability of random packs of monodis-

https://doi.org/10.4208/cicp.210815.240316a Published online by Cambridge University Press

perse spheres: Direct flow simulations versus correlations, Physica A, 389, 205-214.
[33] Wang, Y., S. Sun, and B. Yu (2013), On full-tensor permeabilities of porous media from numerical solutions of the Navier-Stokes equation, Advances in Mechanical Engineering, 137086, 1-11.
[34] Wang, Y. (2011), Essential consistency of pressure Poisson equation method and projection method on staggered grid, Appl. Math. Mech., 32, 789-794.

https://doi.org/10.4208/cicp.210815.240316a Published online by Cambridge University Press